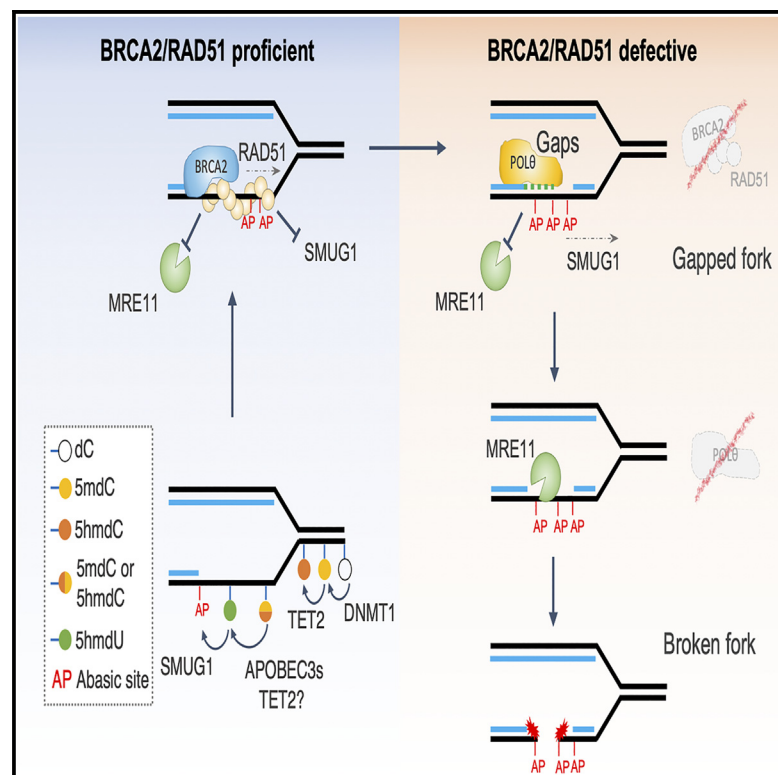# RAD51 protects abasic sites to prevent replication fork breakage

Graphical abstract

Authors

Yodhara Wijesekara Hanthi,
Miguel Angel Ramirez-Otero,
Robert Appleby, ..., Daniele Fachinetti,
Luca Pellegrini, Vincenzo Costanzo

Correspondence

lp212@cam.ac.uk (L.P.),
vincenzo.costanzo@ifom.eu (V.C.)

In brief

Hanthi et al. found that RAD51 recognizes and binds to abasic sites. Together with BRCA2, RAD51 prevents the accumulation of abasic site-induced replicative DNA gaps (caused by DNA methylation, oxidation, and deamination) and averts replication fork breakage, resulting from MRE11-dependent abasic site cleavage within single-stranded DNA, thus ensuring genomic stability.

Highlights

- Cryo-EM structure shows that RAD51 specifically recognizes and binds to abasic sites

- RAD51 prevents MRE11-dependent abasic DNA cleavage, suppressing fork breakage

- BRCA2 and RAD51 also restrict the accumulation of abasic sites and replicative gaps

- RAD51 protects abasic sites resulting from DNA methylation, oxidation, and deamination

CellPress

Article

RAD51 protects abasic sites to prevent replication fork breakage

Yodhara Wijesekara Hanthi,[1,5] Miguel Angel Ramirez-Otero,[1,5] Robert Appleby,[3,5] Anna De Antoni,[1] Luay Joudeh,[3] Vincenzo Sannino,[1] Salli Waked,[1] Alessandra Ardizzoia,[1] Viviana Barra,[4] Daniele Fachinetti,[4] Luca Pellegrini,[3,*] and Vincenzo Costanzo[1,2,6,*]

[1]IFOM, The AIRC Institute of Molecular Oncology, Milan, Italy
[2]Department of Oncology and Hematology-Oncology, University of Milan, Milan, Italy
[3]Department of Biochemistry, University of Cambridge, Cambridge CB2 1GA, UK
[4]Institute Curie, PSL Research University, CNRS, UMR 144, 26 Rue d'Ulm, 75005 Paris, France
[5]These authors contributed equally
[6]Lead contact
*Correspondence: lp212@cam.ac.uk (L.P.), vincenzo.costanzo@ifom.eu (V.C.)
https://doi.org/10.1016/j.molcel.2024.07.004

SUMMARY

Abasic sites are DNA lesions repaired by base excision repair. Cleavage of unrepaired abasic sites in single-stranded DNA (ssDNA) can lead to chromosomal breakage during DNA replication. How rupture of abasic DNA is prevented remains poorly understood. Here, using cryoelectron microscopy (cryo-EM), *Xenopus laevis* egg extracts, and human cells, we show that RAD51 nucleofilaments specifically recognize and protect abasic sites, which increase RAD51 association rate to DNA. In the absence of BRCA2 or RAD51, abasic sites accumulate as a result of DNA base methylation, oxidation, and deamination, inducing abasic ssDNA gaps that make replicating DNA fibers sensitive to APE1. RAD51 assembled on abasic DNA prevents abasic site cleavage by the MRE11-RAD50 complex, suppressing replication fork breakage triggered by an excess of abasic sites or POLθ polymerase inhibition. Our study highlights the critical role of BRCA2 and RAD51 in safeguarding against unrepaired abasic sites in DNA templates stemming from base alterations, ensuring genomic stability.

INTRODUCTION

Abasic sites, referred to as apurinic and apyrimidinic (AP) sites, are among the most frequent DNA lesions.[1] AP sites are predominantly repaired by base excision repair (BER) via AP endonuclease (APE1)-mediated DNA strand incision and subsequent gap filling within double-stranded (ds)DNA.[2] AP sites can arise through spontaneous hydrolysis of the base-sugar bond and following the removal of altered bases by BER glycosylases.

Considerable amounts of AP sites can be generated by demethylation of 5-methyl-2′-deoxycytidine (5mdC) through ten-eleven translocation (TET) methylcytosine dioxygenases that create intermediates like 5-hydroxy-methyl-2′-deoxycytidine (5hmdC), 5-formyl-2′-deoxycytidine (5fdC), and 5-carboxyl-2′-deoxycytidine (5cadC), which thymine DNA glycosylase (TDG) can remove when these are paired with guanine.[3] Single-strand selective monofunctional uracil DNA glycosylase (SMUG1) can instead remove uracil or 5-hydroxymethyl-uracil (5hmU) from single-stranded (ss) in addition to dsDNA,[4,5] possibly arising from base deamination and/or oxidation,[6] forming AP sites[3] that must be carefully processed to avoid replication fork damage.

Unrepaired DNA base damage and AP sites confer toxicity to homologous recombination (HR)-defective cells.[7–13]

DNA synthesis arrest and restart at DNA polymerase stalling lesions results in ssDNA gaps trailing behind replication forks in the absence of HR factors RAD51 and BRCA1/2.[13–21]

SMUG1 plays a major role in ssDNA gap formation in the absence of functional HR proteins.[13] However, the mechanisms responsible for the accumulation of ssDNA gaps during DNA replication in the absence of HR proteins remain elusive. Furthermore, it is yet to be determined if HR proteins have a direct influence on AP sites, apart from their established role in repairing double-strand breaks (DSBs) that might result from the processing of these lesions. Addressing these questions is challenging due to the essential role of key HR factor RAD51.

Here, we employed a multidisciplinary approach including cryoelectron microscopy (cryo-EM) imaging and reconstruction of RAD51 nucleoprotein filaments (NPFs), biochemical assays with purified proteins, *Xenopus laevis* (*Xl*) egg extracts, and DNA EM to study the mechanisms underlying HR factors-mediated control of AP-site metabolism.

We also developed a new method to identify AP sites within ssDNA gaps occurring at replication forks. This technique is

useful to highlight the presence of spontaneous AP sites in replicating templates isolated from HR-defective cancer cells.

Our results demonstrate that RAD51 can directly recognize AP sites by exploiting its natural binding mechanism to DNA and that the presence of AP sites increases RAD51's association rate with DNA, protecting AP sites from uncontrolled processing and suppressing their accumulation. These functions of RAD51 are critical in preventing replication fork breakage caused by excessive AP sites, especially when compensatory mechanisms, including POLθ polymerase-dependent abasic ssDNA gap filling, are impaired.

Remarkably, the accumulation of abasic ssDNA gaps and fork breakage can be suppressed by inhibiting TET2 oxidase, APOBEC3B deaminase, or DNA methyltransferase 1 (DNMT1), highlighting enzymatic base modifications as a major source of AP sites that lead to the accumulation of ssDNA gaps in HR-defective vertebrate cells.

RESULTS

Structural basis for the recognition of abasic DNA by RAD51

In the cryo-EM structure of the RAD51 NPFs, the phospho-ribose backbone of DNA is embedded within a protein sheath of helically arranged RAD51 molecules, whereas the bases project out toward the solvent.[22] The DNA-binding loops L1 and L2 of RAD51 grip the phospho-ribose backbone, unstacking the bases of filament DNA into triplets of nucleotides that remain in approximate B-DNA conformation. Given its mode of DNA interaction, we reasoned that RAD51 binding to abasic DNA should be possible or even more favorable compared with normal DNA. Thus, the gap in the DNA caused by the missing base would constitute a preferential site of filament nucleation, as the bases flanking the AP site are already unstacked. Electrophoretic mobility shift assays indicated that RAD51 can form NPFs with ss- and ds-DNA containing abasic DNA sites with equivalent apparent affinity as with normal DNA (Figures S1A and S1B). Furthermore, kinetic analysis of binding using surface plasmon resonance showed that the rate of RAD51 association with DNA oligonucleotides increases in proportion to the number of abasic sites present in the sequence (Figures 1A and S1C). Biochemical evidence supported a model whereby RAD51 would preferentially bind to the AP site with its DNA-binding loops L1 and L2 rather than unstacking the bases of adjacent nucleotides. We tested this hypothesis by cryo-EM structure determination of a RAD51 NPF containing a ssDNA oligonucleotide with multiple abasic sites positioned 3-nt apart to match the known footprint of RAD51 on DNA.[22] We reasoned that if RAD51 did bind preferentially to the regularly spaced AP sites in the DNA sequence, the filament structure determined by helical averaging would show no density for the base of the nucleotide recognized by loops L1 and L2 of each RAD51 protomer. Alternatively, if RAD51 bound indifferently to abasic or normal sites, helical averaging would yield the same density for the base of all nucleotides in the filament. The 3.2 Å cryo-EM structure of a RAD51 NPF bound to a 23-nt oligonucleotide with 7 regularly spaced AP sites showed the complete absence of density for the base of the nucleotide

engaged by RAD51 loops L1 and L2 (Figures 1B, 1C, S2A, and S2B; Table 1). Thus, the experiment proved that the AP sites had determined the position of the RAD51 protomers on filament DNA, in support of a preference for RAD51 binding to AP sites. In the structure, RAD51 binds abasic ssDNA in a similar way as observed for the structure of the pre-synaptic filament,[23] except that the N-terminal segment of loop L2 has shifted to partially occupy the gap of the missing base with the side chain of V273 (Figures 1D and 1E).

AP sites can occur on both ss- and ds-DNA. We sought to determine if RAD51 can recognize AP sites in the context of dsDNA, and whether it showed preference for the DNA strand carrying AP sites within a DNA double helix. We reconstituted a RAD51 NPF on dsDNA using the same oligonucleotide carrying regularly spaced AP sites that had been annealed to its complementary sequence with no abasic sites. To stabilize short dsDNA, we reduced the number of AP sites to the central five, so that each end would have 5-nt long tracts of normal dsDNA. Cryo-EM structure determination of this filament by helical averaging at 3.6 Å showed strongly reduced density for the base at the nucleotide position of the inner strand recognized by RAD51 loops L1 and L2, whereas the outer strand of dsDNA in the filament showed density for a full complement of bases (Figures 2A, 2B, S3A, and S3B; Table 1). Overall, RAD51 interacts with the abasic dsDNA in a highly similar mode as in the post-synaptic filament (Figures 2C and 2D).[23]

This experiment demonstrated the same mode of RAD51 binding to AP sites in dsDNA observed for abasic ssDNA. It further showed that RAD51 can discriminate between abasic and normal DNA strands within the double helix, by preferentially binding the abasic strand.

AP sites stimulate RAD51 chromatin recruitment

To validate RAD51's binding to AP sites, we analyzed RAD51 chromatin association in *Xl* egg extract following APE1 inhibition using AR03[26] and APE1 inhibitor III (APE1i).[27,28] These treatments increased RAD51 chromatin binding without causing DNA DSBs, as evidenced by the absence significant levels of phosphorylated histone H2AX (γH2AX) in the treated samples (Figures 3A and 3B) and the lack of ataxia telangiectasia and Rad3-related (ATR) chromatin enrichment normally induced by stalled and broken replication forks.[15] The presence of AP sites was confirmed using a biotinylated aldehyde reactive probe (ARP),[29] which detected more AP sites in nuclei treated with APE1i (Figures 3C and 3D). Control experiments with sperm nuclei treated with non-saturating amounts of methyl methane sulfonate (MMS)[14] validated the ARP's detection of AP sites (Figures 3C and 3D). A complementary enzyme-linked immunosorbent assay (ELISA) conducted on genomic DNA isolated from treated extracts corroborated AP-site induction (Figure 3E).

To validate the effects of APE1 inhibition on RAD51 chromatin recruitment, we produced *Xl* SMUG1 (xSMUG1) (Figure S4A), a DNA glycosylase that removes uracil from ssDNA, creating AP sites.[4,5,30] xSMUG1's activity was confirmed *in vitro* with active recombinant *Xl* APE1 (xAPE1) (Figure S4B), which was capable
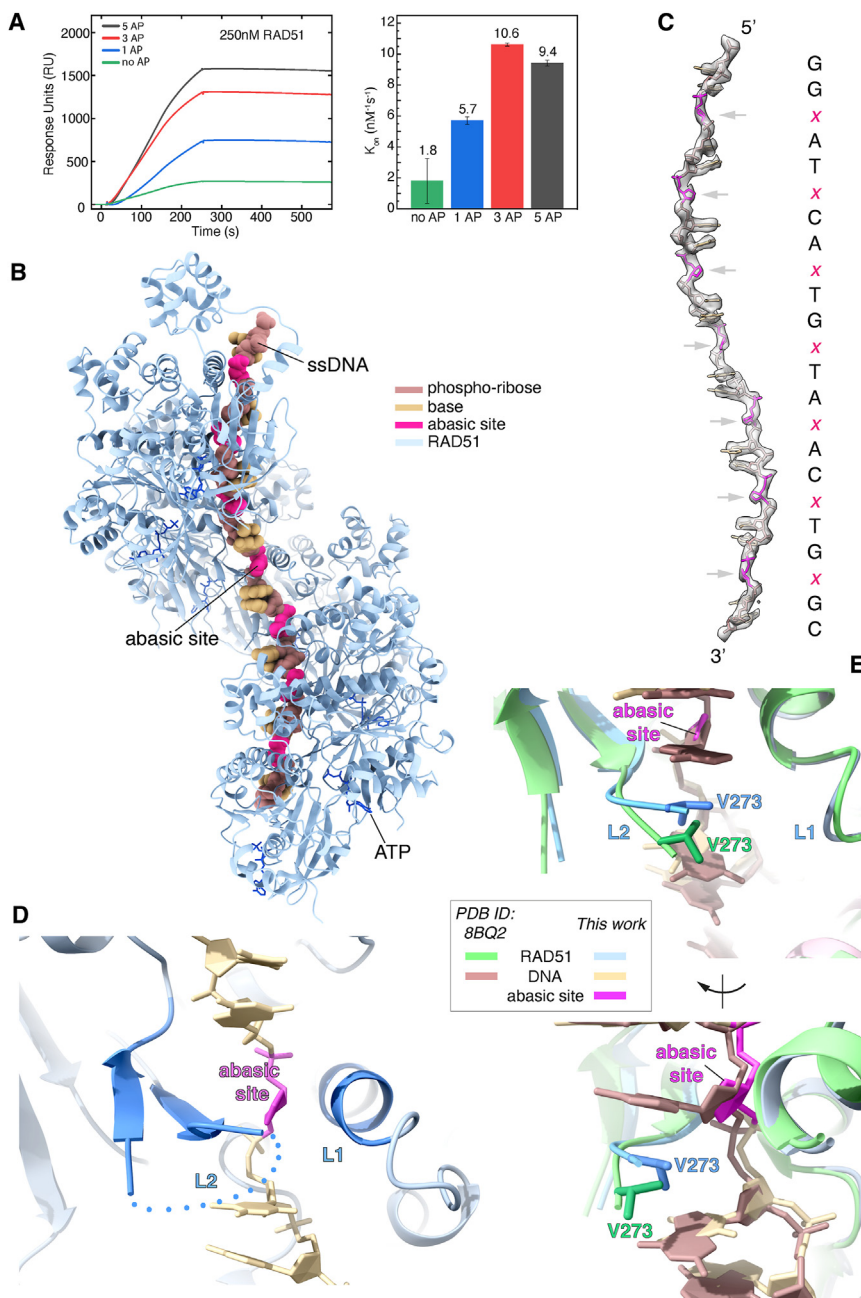
Figure 1. RAD51 binds to ssDNA containing abasic sites

(A) Surface plasmon resonance analysis of RAD51's interaction with abasic ssDNA. The biotinylated DNA ligand was coupled to a streptavidin-coated sensor chip, and the RAD51 analyte was added to the mobile phase to measure the RU response. The left panel shows representative sensorgrams of RAD51 binding to DNA oligonucleotides with 1, 3, and 5 AP sites, and no AP sites as control. The right panel reports the apparent association rates (K_{on}) of RAD51 to the abasic DNA oligonucleotides, from sensogram data analysis.

(B) Cryo-EM structure of a RAD51 nucleoprotein filament with ssDNA containing multiple, periodically spaced AP sites (AP7). The RAD51 protomers in the filament are drawn as ribbons and the ssDNA is in spacefill representation.

(C) Cryo-EM density of the ssDNA in the filament, with fitted oligonucleotide structure. The abasic nucleotides are colored pink and their position is indicated by an arrow. The DNA sequence is shown next to the structure; abasic site positions are marked by x.

(D) RAD51's DNA-binding loops L1 and L2 interaction with the AP site. Loops are drawn as light blue ribbons, while the DNA is in light-brown filled-ring representation with the abasic nucleotide colored pink.

(E) Superposition of pre-synaptic RAD51 NPF (PDB: 8BQ2) with the NPF on abasic ssDNA (this work). Two rotated views of the filament are shown, centered on the position of the AP site.

See also Figures S1 and S2.

of cleaving an AP site-containing oligo (Figure S4C) and an uracil-containing oligo exposed to xSMUG1 (Figure S4D).

An excess xSMUG1 enhanced RAD51's chromatin binding, exceeding the levels induced by aphidicolin (APH)[15] or SMUG1/APH combination, indicating a rise in AP site formation akin to APE1 inhibition (Figures 3F and 3G).

RAD51 discriminates abasic strands within dsDNA (Figures 2A–2D). Using geminin to halt DNA replication and unwinding,[31] we observed that xSMUG1-generated AP sites in dsDNA also enhanced RAD51's chromatin binding, suggesting that AP sites promote RAD51 recruitment beyond ssDNA contexts (Figures 3H and 3I).

RAD51-dependent protection of abasic DNA from nuclease-mediated cleavage

To evaluate AP sites' impact on replicating genomes, we examined DNA replication forks isolated from APE1i or SMUG1-treated extracts using EM.[14,15,32] These agents induced ssDNA gaps, increasing the total length of ssDNA accumulating at replication forks (Figures 4A, 4B, and S4E). Inhibiting RAD51 DNA binding with GST-BRC4 peptide (BRC4) led to larger ssDNA gaps on intact forks, possibly from MRE11 exonuclease activity on nascent DNA[14,15,32] (Figures 4B, 4C, S4F, and S4G).

Remarkably, APE1i or SMUG1 treatment with BRC4 led to breaks in nearly 50% of forks, as shown by the presence of asymmetric branches, indicating severing of one of the replicated arms[15] (Figures 4D, 4E, S4F, and S4G). Frequent breaks on gapped strands (Figures 4D, S4F, and S4G) suggest that ssDNA gaps evolved into DSBs.[15]

To determine the fork breakage mechanism, we examined nucleases present at forks known to cut AP sites. The human MRE11-RAD50 (MR) complex[33] could cleave AP sites from

Table 1. Cryo-EM data collection and real-space refinement

Data collection

–	Abasic ssDNA NPF (EMDB: EMD-19050, PDB: 8RCD)		Abasic dsDNA NPF (EMDB: EMD-19051, PDB: 8RCF)	
Microscope	Titan Krios G3			
Voltage (keV)	300			
Detector	Gatan K3			
Collection mode	counting			
Magnification	130,000×			
Defocus range (μm)	−2.6, −2.4, −2.2, −2.0, −1.8, −1.6, −1.4, −1.2, −1.0, −0.8			
No. movies	10,623		10,084	
Frames/movie	49		44	
Pixel size (Å/pixel)	0.652			
Electron dose ($e^-/Å^2/s$)	41.5		44.14	
Exposure (s)	1.33		1.20	
Picked particles	851,378		1,791,680	
Final particles	183,769		8853	
Processing method	helical reconstruction			
asm units (#)	6			
Helical twist (°)	56.3		56.0	
Helical rise (Å)	16.2		15.8	
Resolution estimates (Å)	Masked	Unmasked	Masked	Unmasked
d_{FSC} (half maps; 0.143)	3.2	3.4	3.6	3.8
d_{99} (full/half1/half2)	3.1/4.2/4.2	3.0/3.7/3.7	3.6/2.7/2.7	3.6/2.7/2.7
d_{model}	3.2	3.2	3.5	3.5
$d_{FSC\ model}$ (0/0.143/0.5)	2.9/3.0/3.3	2.9/3.0/3.5	3.2/3.3/3.6	3.2/3.4/3.8

Real-space refinement

–	Abasic ssDNA NPF	Abasic dsDNA NPF
Composition		
Chains	9	10
Atoms	19,680 (hydrogens: 0)	20,202 (hydrogens: 0)
Residues	protein: 2,480 nucleotide: 23	protein: 2,488 nucleotide: 46
Water	0	0
Ligands	Ca: 16, ATP: 8	Ca: 16, ATP: 8
Model		
Bonds (RMSD)		
Length (Å) (# > 4σ)	0.009 (0)	0.008 (2)
Angles (°) (# > 4σ)	0.615 (0)	0.629 (0)
MolProbity score[24]	2.04	1.74
Clash score	11.65	9.12
Ramachandran plot (%)		
Outliers	0.0	0.0
Allowed	7.19	1.47
Favored	92.81	98.53
Rotamer outliers (%)	0.05	2.16
Cbeta outliers (%)	0.0	0.0
ADP (B factors)		
Iso/Aniso (#)	19,680/0	20,202/0

Table 1. Continued

Data collection		
–	Abasic ssDNA NPF (EMDB: EMD-19050, PDB: 8RCD)	Abasic dsDNA NPF (EMDB: EMD-19051, PDB: 8RCF)
min/max/mean		
Protein	25.79/122.15/65.94	62.75/129.35/91.93
Nucleotide	55.91/63.38/58.35	40.27/193.54/75.20
Ligand	47.74/64.34/55.28	50.09/86.04/82.91
Model vs. data		
CC mask[25]	0.85	0.77
CC box	0.58	0.58
CC peaks	0.52	0.45
CC volume	0.83	0.76
Mean CC for ligands	0.87	0.83

UDG-treated ssDNA oligos,[34] matching human APE1 efficiency (Figure S4H).

The MRE11 endonuclease inhibitor PFM01[35] reduced broken forks induced by AP-site accumulation in the absence of RAD51 bound to DNA, implicating MRE11 in cleaving abasic ssDNA gaps (Figures 4E and 4F). PFM01 also reduced fork breakage induced by SMUG1 excess without RAD51 (Figures 4E and S4I). RAD51 inhibited both MR complex and APE1-dependent cleavage of AP site-containing oligos (Figures 4G, 4H, and S4J), suggesting that RAD51 NPFs block nuclease access to DNA.

As POLθ can bypass AP sites[36] and fill ssDNA gaps,[15,21] we verified abasic gap sealing by POLθ. Adding a 2.5-fold excess of the full length of *Xl* POLθ[15] to egg extract reduced ssDNA gaps and fork breakage induced by APE1i or xSMUG1 treatment in the absence of RAD51 bound to DNA (Figures 4B and 4E).

Overall, these findings suggest that RAD51 binding and POLθ-mediated DNA synthesis across AP sites prevent abasic gaps conversion to DSBs.

AP sites trigger ssDNA gaps in APEX1- or BRCA2-defective cells

To verify whether AP sites are directly linked to spontaneous ssDNA gaps that occur during DNA replication in the absence of RAD51 bound to DNA, we set up a novel assay based on replicating DNA fibers analysis coupled with APE1 nuclease treatment (Figures 5A and 5B). Unlike S1 nuclease,[37] APE1 shortens DNA fibers only when encountering AP sites containing ssDNA (Figure 5A), allowing the detection of AP sites in replicating DNA templates.

To conduct the APE1-fiber assay, replication forks were sequentially labeled with chloro-deoxyuridine (CldU) and iodo-deoxyuridine (IdU) base analogs. Permeabilized nuclei were then exposed to APE1 or S1 nucleases (Figure 5B), which were equally able to shorten IdU tracts on DNA fibers isolated from APE1i-exposed DLD1 wild-type (WT) cells, indicating the presence of AP site-containing ssDNA gaps (Figure 5B). Noticeably, APE1i reduced fork speed as shown by shorter IdU track lengths even without enzyme treatment, consistent with AP sites' ability to decrease fork progression[38] (Figure 5B).

Genome-wide rise in AP sites from APE1i was confirmed with AA3, a cell-permeable alkoxyamine that tags endogenous AP sites that can be fluorescently labeled via click chemistry for AP-site quantification on either nascent or parental DNA.[39] AA3 fluorescence increased with APE1i concentration, confirming AP-site accumulation (Figures S5A and S5B). Nuclear fluorescence, concentrated in areas potentially more prone to AP sites formation,[40] was evident even at low APE1i doses (Figure S5B).

To validate the results obtained with APE1i, we used CRISPR-Cas9 to generate APEX1$^{-/-}$ DLD1 cells (Figure S5C), which showed increased unrepaired AP sites, as measured by ELISA and AA3 fluorescence (Figures 5C–5E). As expected, APE1i did not increase toxicity in APEX1$^{-/-}$ cells any further, unlike in BRCA2$^{-/-}$ cells, which were APE1i sensitive (Figure S5D).

IdU tracks on fibers from APEX1$^{-/-}$ cells were shorter after APE1 or S1 nuclease treatment, confirming the formation of abasic ssDNA gaps in the absence of APE1 activity (Figure 5F).

Importantly, both BRCA2$^{-/-}$ cells and those with silenced BRCA2 or RAD51 showed IdU-labeled fiber shortening following APE1 treatment (Figures 5F, S5E, and S5F). This effect was absent in CldU-labeled segments replicated earlier (Figure S5G). These results suggest that AP sites within ssDNA gaps arise in the proximity of active replication forks in the absence of RAD51 or BRCA2 and are sealed as replication forks progress.

SMUG1 knockdown, confirmed by immunoblot (Figure S5H), suppressed abasic ssDNA gaps in APEX1$^{-/-}$ and BRCA2$^{-/-}$ DLD1 cells (Figure 5G) and APE1i-treated WT cells (Figure S5I), indicating a key role for SMUG1 in abasic ssDNA gap formation. SMUG1 knockdown also slowed fork progression in cells with intact APEX1 (Figures 5G and S5I), likely due to the accumulation of uncleared modified bases, a phenomenon that remains to be further defined.

BRCA2- and RAD51-mediated suppression of AP sites

Surprisingly, AP sites were more prevalent in BRCA2$^{-/-}$ than WT or APEX1$^{-/-}$ cells (Figures 5C–5E and S5J) and in *Xl* nuclei with compromised RAD51 chromatin binding (Figures S5K and S5L), indicating that DNA-bound RAD51 may inhibit AP-site accumulation.
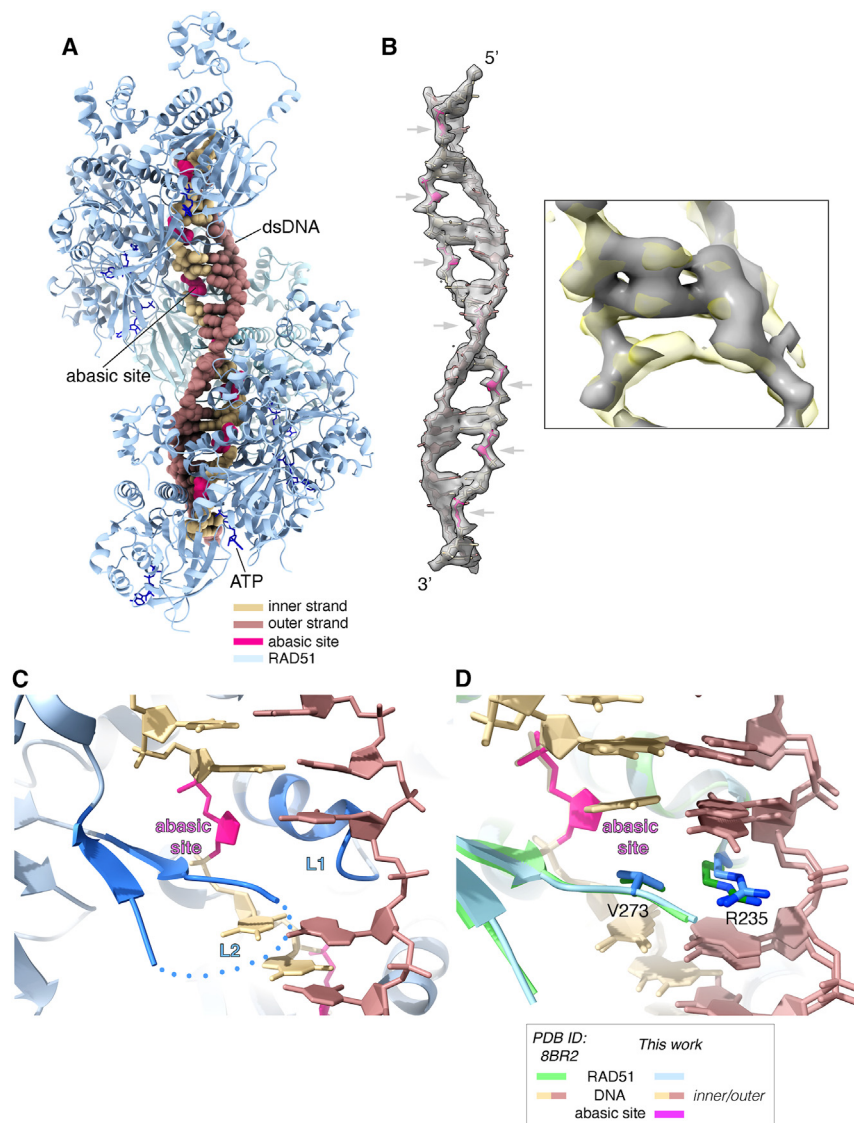
Figure 2. RAD51 binds to the abasic strand in dsDNA

(A) Cryo-EM structure of a RAD51 nucleoprotein filament containing abasic ssDNA (AP5) annealed to its complementary DNA sequence (APc).

(B) Cryo-EM density of the dsDNA in the filament, with fitted dsDNA structure. Abasic nucleotides are colored in pink. Their position is indicated by an arrow. Inset on the right shows a superposition of cryo-EM maps for abasic dsDNA (this work) in gray and dsDNA in the post-synaptic RAD51 filament[23] in transparent yellow. The weak density still visible at the AP site position is the result of helical averaging including normal nucleotides at the two outermost positions in the AP5-APc dsDNA, so that a residual signal corresponding to 2/7 of normal base density would be expected for exclusive recognition of AP sites by RAD51.

(C) Interaction of RAD51's DNA-binding loops L1 and L2 with the AP site in dsDNA. Loops are drawn as light blue ribbons. DNA is in filled-ring representation, colored light- and dark brown for the inner and outer DNA strands respectively, with the abasic nucleotide colored pink.

(D) Superposition of post-synaptic RAD51 NPF (PDB: 8BR2) with the NPF on abasic dsDNA (this work).

See also Figure S3.

POLθ significantly contributes to sealing abasic ssDNA gaps (Figure S5M).

Silencing of DNA-directed primase/polymerase protein (PRIMPOL) (Figures S6A and S6B), crucial for DNA synthesis restart and ssDNA gap formation without BRCA1/2,[13,19,20] significantly reduced abasic ssDNA gaps in APEX1^{−/−} and BRCA2^{−/−} cells and in those treated with APE1i (Figures S6C–S6F). PRIMPOL was required for normal fork progression in these contexts due to its AP-site bypass ability.

POLθi did not further increase AP-site gaps in PRIMPOL-inactivated APEX1^{−/−} cells, suggesting that POLθ fills gaps post-PRIMPOL synthesis (Figure S6C). Conversely, POLθi prevented full suppression of gaps mediated by PRIMPOL knockdown in BRCA2^{−/−} cells, indicating that POLθ fills PRIMPOL-independent abasic gaps arising in this context (Figure S6D), possibly on the lagging strand.[15]

To further verify the occurrence of SMUG1- and PRIMPOL-dependent abasic ssDNA gaps in BRCA2-deficient conditions, we used PEO1 cancer cells with a mutation producing a non-functional truncated BRCA2 (BRCA2[Y1655X]) and PEO1 reversion cells (C4-2) with restored BRCA2 (BRCA2[WT])[41,42] (Figure S6G). APE1- and S1-dependent DNA fiber shortening was observed only in mutant cells and was abolished by SMUG1 or PRIMPOL knockdown (Figure S6H), confirming abasic gap formation in these tumor cells.

Abasic site processing protein (HMCES) also protects DNA from AP sites during replication.[28] Accordingly, inhibition of

Accordingly, uracil-containing ssDNA preincubated with RAD51 resisted AP-site formation by xSMUG1, as shown by the lack of xAPE1-mediated cleavage following RAD51 and SMUG1 inactivation (Figure 5H). This suggests RAD51 shielding of DNA from glycosylase action.
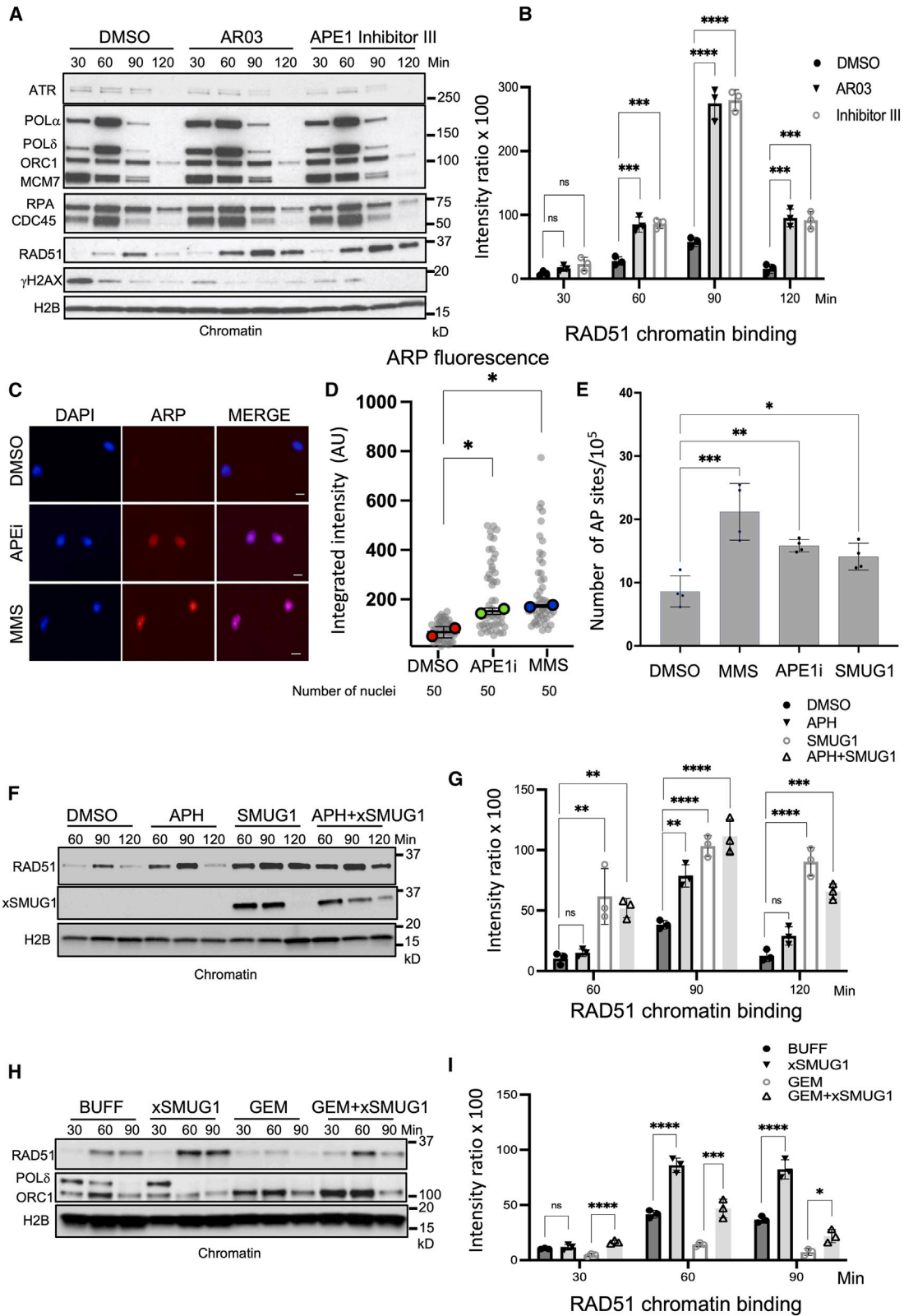
SMUG1 downregulation reduced AP-site accumulation in asynchronously growing BRCA2^{−/−} cells but did not completely suppress it (Figure S5J). This is possibly due to additional processes contributing to SMUG1-independent AP formation in the absence of RAD51 bound to non-replicating dsDNA. However, complete AP-site suppression occurred in APEX1^{−/−} cells, suggesting effective control of an intact BRCA2/RAD51 function over AP sites' accumulation (Figure S5J).

Considering POLθ's ability to bypass AP sites,[36] we explored its role in gap suppression. Inhibiting POLθ polymerase with POLθi, a previously characterized inhibitor,[15,21] increased abasic ssDNA gap formation in APEX1^{−/−} and BRCA2^{−/−} cells, indicating that

(legend on next page)

HMCES expression (Figure S6I) increased abasic gaps in replicating DNA isolated from WT DLD1 cells (Figure S6J). Instead, in BRCA2$^{-/-}$ cells, HMCES silencing reduced fork progression and rendered DNA fibers resistant to S1 and APE1 treatment (Figure S6J). This might be due to the increased recruitment of slower translesion synthesis (TLS) polymerases filling abasic gaps and reducing the fork rate, a process restricted by HMCES.[38] The direct molecular relationship between HMCES and TLS in BRCA2$^{-/-}$ cells remains to be determined.

DNMT1-, APOBEC3B-, and TET2-dependent abasic DNA gap accumulation

To investigate the origin of spontaneous abasic gaps, we explored the possibility that AP sites originate from 5mdC turnover.

To this end, we targeted DNMT1 and DNMT3B DNA methyltransferases.[43] Using auxin-inducible degron (AID) technology,[44] we degraded DNMT1 alone (DNMT1^{NA}) or in combination with DNMT3B knockout (DNMT1^{NA}/DNMT3B$^{-/-}$) in DLD1 cells.[45] Treatment with indole-3 acetic acid (IAA) for 48 h resulted in complete DNMT1 degradation in DNMT1^{NA} (Figure S6K), leading to a 50% reduction in 5mdC levels,[45] significantly restraining AP site-containing ssDNA gaps in BRCA2-silenced cells (Figure 5I). Similar results were obtained by inducing DNMT1 degradation in DNMT3B$^{-/-}$ cells (Figures 5J and S6K), a combination leading to a more pronounced 5mdC loss.[45] These results demonstrate a direct connection between DNA methylation and abasic gap formation in the absence of BRCA2. Accordingly, DNMT1 degradation significantly reduced the excess of total AP sites caused by acute downregulation of BRCA2 in asynchronously growing cells (Figures S6L and S6M).

5mdC is oxidized to 5hmdC by TET enzymes.[3] TET2 knockdown (Figure S7A) suppressed abasic ssDNA gap formation in BRCA2$^{-/-}$ cells (Figure 5K). Conversely, knockdown of TDG (Figure S7B), which removes 5fdC and 5cadC from dsDNA,[3] reduced fork speed possibly due to the accumulation of uncleared modified bases in cells with intact APEX1 (Figure S7C). However, it did not suppress ssDNA gaps in either APEX1$^{-/-}$ or BRCA2$^{-/-}$ DLD1 cells (Figure S7C), indicating that DNA demethylation occurring within dsDNA does not contribute to ssDNA gap accumulation during replication.

The suppression of abasic ssDNA gaps by SMUG1 downregulation, coupled with SMUG1's ability to excise 5hmU,[4,5,30] led us to explore 5-hydroxymethyl-uridine (5hmdU) production mechanisms in ssDNA.

We investigated APOBEC3B deaminase, which *in vitro* can convert 5hmdC to 5hmdU in ssDNA, albeit with low efficiency.[46] Silencing APOBEC3B, present in the nucleus of several cancer cells, including DLD1[47-50] (Figure S7D), significantly reduced abasic ssDNA gap formation (Figure S7E). Additional APOBEC3 members expressed in DLD1 and other cancer cells, such as APOBEC3C, D, F, and H,[47-50] may jointly contribute to the accumulation of abasic gaps.

MRE11-dependent cleavage of AP sites at replication forks in BRCA2- and RAD51-defective cells

We then assessed AP sites' impact on replicating genomes in BRCA2$^{-/-}$ cells. APE1i induced DSBs in BRCA2$^{-/-}$ DLD1 cells, mostly in S-phase, as evidenced by γH2AX foci accumulation in EdU-positive and in a few non-S-phase cells (Figures 6A and 6B). MRE11 inhibition with PFM01 or MRE11 knockdown reduced γH2AX foci induced by APE1i in BRCA2$^{-/-}$ and BRCA2-silenced APEX1$^{-/-}$ cells (Figures 6A, 6B, and S7F–S7J). These results indicate that in human cells, an overload of AP sites induced by APE1 inhibition is not tolerated in the absence of RAD51 bound to DNA, similar to *Xl*.

DNA EM confirmed APE1i-induced breakage in replication forks isolated from BRCA2$^{-/-}$ DLD1 cells, suppressed by PFM01 (Figures 6C and 6D). These observations indicate that BRCA2 and RAD51 protect against fork breakage induced by AP site-cleaving nucleases and align with the known synthetic lethality between APEX1 and BRCA2.[8]

We then tested POLθ's role in mitigating fork breakage. We monitored γH2AX accumulation in WT and APEX1$^{-/-}$ cells exposed to POLθi following RAD51 or BRCA2 small-interfering RNA (siRNA)-mediated knockdown (Figures 6E, 6F, S7K, and S7L). POLθ polymerase inhibition further augmented γH2AX foci formation triggered by defective APEX1, RAD51, or BRCA2 (Figures 6E, 6F, S7M, and S7N). Consistent with these findings, APEX1$^{-/-}$ cells exhibited high sensitivity to POLθi (Figure S7O), although the effect was less pronounced compared

---

Figure 3. RAD51 recruitment by AP sites containing chromatin

(A) Representative immunoblot of chromatin assembled with sperm nuclei (4,000 n/μL), incubated in egg extract treated with DMSO, AR03 (10 μM), or APE1 inhibitor III (10 μM) and isolated at indicated times.

(B) Quantification of RAD51 chromatin binding as in (A) normalized to H2B. Horizontal bars indicate mean ± SD. Symbols indicate n = 3 independent biological replicate values. One-way ANOVA, followed by Dunnett's post hoc test for multiple comparisons; ***p < 0.001; ****p < 0.0001.

(C) Immunofluorescence of sperm nuclei treated with MMS (3 mg/mL) or APE1i, stained with DAPI and ARP, and detected with fluorescent avidin.

(D) Quantification of (C) showing individual nuclei intensity. Horizontal bars indicate mean ± SD of all data points. Overlay dots indicate independent n = 2 biological replicate medians. One-way ANOVA, followed by Dunnett's post hoc test; *p < 0.05.

(E) ELISA quantification of AP sites in DNA from treated extracts. Horizontal bars indicate mean ± SD of all data points. Overlay dots indicate n = 4 independent biological replicate values. One-way ANOVA, followed by Dunnett's post hoc test; *p < 0.05; **p < 0.01; ***p < 0.001.

(F) Immunoblot of chromatin derived from extracts treated with DMSO, APH (1.5 mM), recombinant xSMUG1 (0.5 μM), or both for the indicated times. His-tagged SMUG1 detected.

(G) Quantification of RAD51 chromatin binding as in (F) normalized to H2B. Horizontal bars indicate mean ± SD. Symbols indicate n = 3 independent biological replicate values. One-way ANOVA, followed by Dunnett's post hoc test; **p < 0.01; ***p < 0.001; ****p < 0.0001.

(H) Immunoblot of chromatin derived from extracts treated with buffer, xSMUG1, GEMININ (GEM) (25 ng/μL), or both for the indicated times.

(I) Quantification of RAD51 chromatin binding as in (H) normalized to H2B. Horizontal bars indicate mean ± SD. Symbols indicate n = 3 independent biological replicate values. One-way ANOVA, followed by Dunnett's post hoc test; **p < 0.01; ***p < 0.001; ****p < 0.0001.
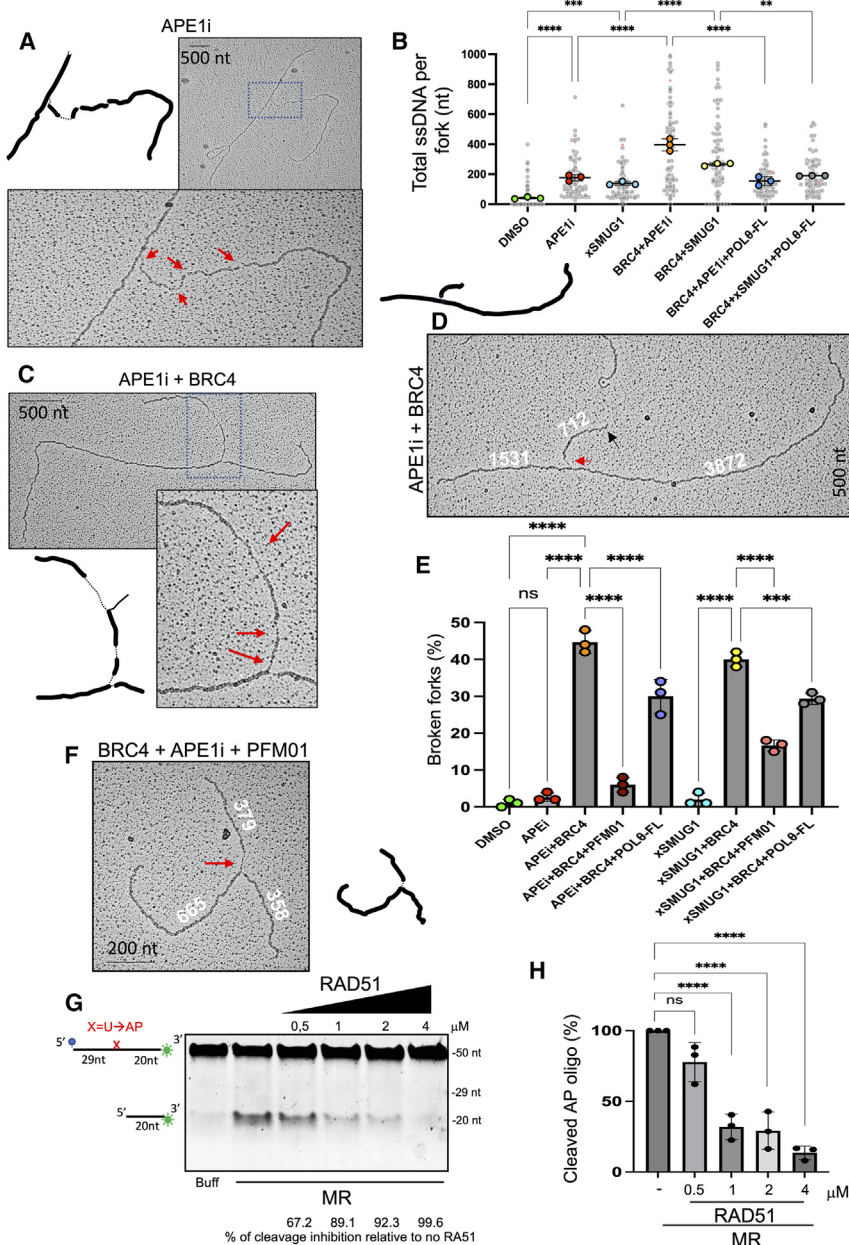
See also Figure S4.

Figure 4. RAD51-mediated protection against MRE11-dependent abasic DNA processing and fork breakage

(A) Representative EM image of a replication fork from egg extract treated with APE1i (10 μM, 45 min). Magnified area in rectangle. Cartoon dotted lines show ssDNA.

(B) Quantification of total ssDNA length for each fork isolated from extracts treated as indicated. Horizontal bars indicate the mean ± SD for a total of 72 forks. Overlay dots show $n = 3$ independent biological replicate means. One-way ANOVA, followed by Tukey's post hoc test for multiple comparisons; $^{**}p < 0.01$; $^{***}p < 0.001$; $^{****}p < 0.0001$.

(C and D) Representative EM images of forks from an extract treated with APE1i (10 μM) and GST-BRC4 (0.5 mg/mL, 45 min).

(E) Percentage of broken forks from extracts treated as indicated. Horizontal bars indicate mean ± SD relative to 72 forks. Overlay dots show $n = 3$ independent biological replicate means. One-way ANOVA, followed by Tukey's post hoc test; $^{**}p < 0.01$; $^{***}p < 0.001$; $^{****}p < 0.0001$.

(F) EM of a rescued fork from extract treated with APE1i, GST-BRC4, and PFM01 (100 μM). Base pair lengths numbered; gaps by red arrows; broken arm by black arrow.

(G) Denaturing gel showing fluorescein-labeled ssDNA with an AP-site generated by UDG-mediated uracil removal and treatment with buffer or 200 nM MR complex and increasing RAD51.

(H) AP oligo cleavage percentage in the presence of MR and increasing RAD51. No RAD51 sample was taken as reference. Horizontal bars indicate mean ± SD of all data points. Overlay dots show $n = 3$ independent replicates. One-way ANOVA, followed by Dunnett's post hoc test; $^{****}p < 0.0001$; ns, non-significant.

See also Figure S4.

with BRCA2$^{-/-}$ cells. These findings suggest BRCA2, RAD51, and POLθ counteract fork breakage from endogenous AP sites.

Remarkably, reducing DNA methylation prevented γH2AX foci increase induced by POLθi in BRCA2-silenced cells (Figures 6G and 6H), implying that base changes derived from methylated DNA promote DSB formation in the absence of BRCA2 and POLθ polymerase activity.

DISCUSSION

RAD51 plays an essential role in higher eukaryotes due to its requirement for HR-based DSB repair.[51–53] However, its function in unchallenged DNA replication has also been increasingly

recognized. The absence of functional HR proteins results in the accumulation of ssDNA gaps during chromosomal DNA replication. This suggests additional roles for RAD51 that are independent of DSB repair.[13–19] The origin and fate of these gaps remain unclear to date.

Our study shows that RAD51 suppresses ssDNA gaps' accumulation by regulating AP-site metabolism. We demonstrate that (1) RAD51 specifically recognizes AP sites, as shown through cryo-EM-mediated visualization of RAD51 NPFs; (2) the presence of AP sites increases RAD51's DNA association rate; (3) RAD51 NPFs preferentially form on abasic DNA strands; (4) RAD51 NPFs hinder abasic DNA processing by AP nucleases, preventing replication fork breakage caused by MRE11-dependent cleavage of unrepaired AP sites; (5) APE1 treatment of DNA fibers reveals gaps containing AP sites in replicating DNA templates; (6) BRCA2 and RAD51 reduce AP site and abasic gaps' accumulation by limiting glycosylases access to DNA; (7) POLθ seals abasic gaps limiting DSB formation; and (8)
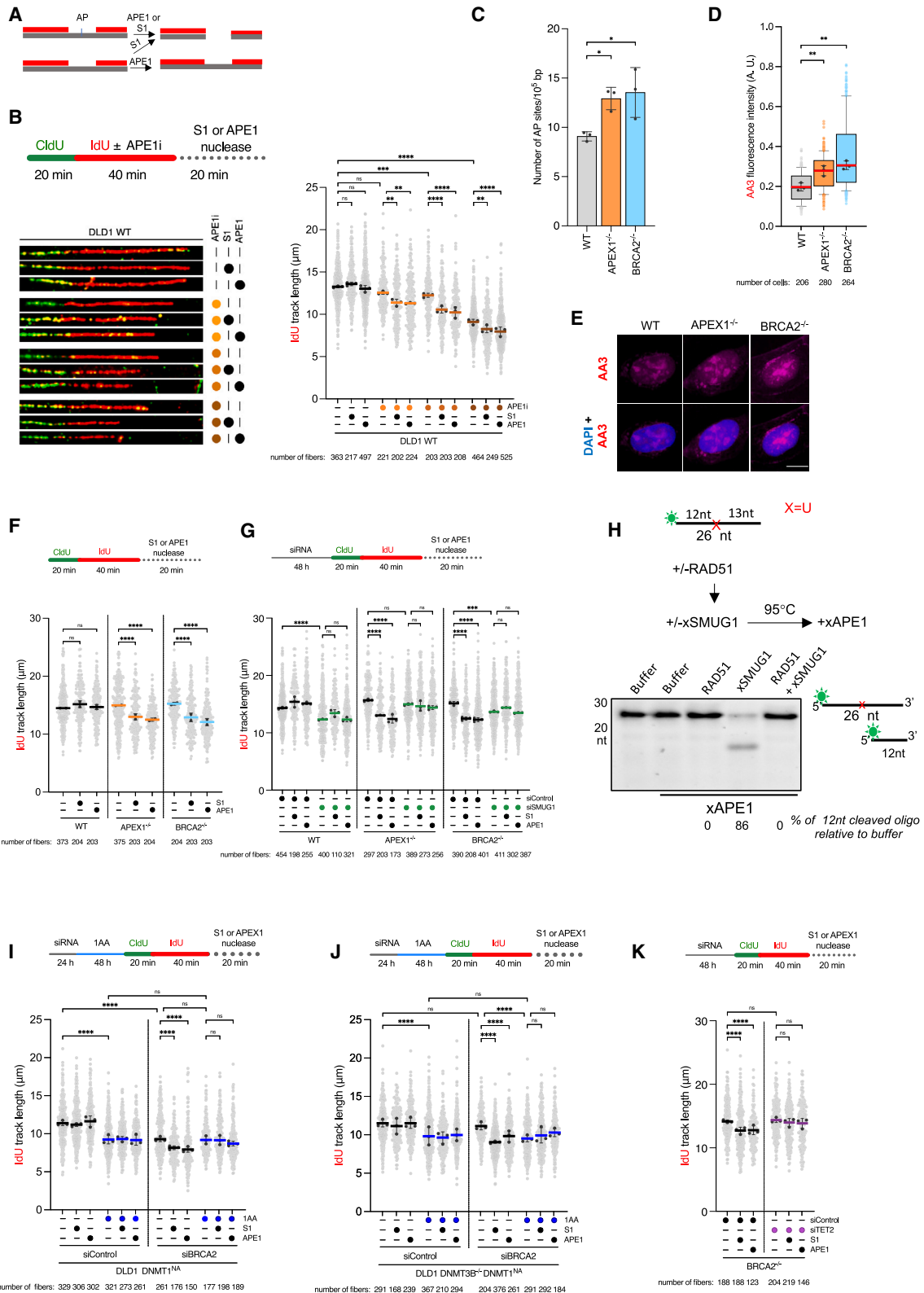
(legend on next page)

DNMT1, TET2, APOBEC3B, and SMUG1 contribute to abasic gaps formation and fork breakage.

Collectively, these results provide new insights into HR proteins' role in genome stability.

Structural determinants of AP-site recognition

We demonstrate that RAD51 NPFs specifically recognize AP sites in both ss- and ds-DNA. This preference is related to RAD51's DNA-binding mechanism, wherein the L1 and L2 loops from its ATPase domain unstack bases into nucleotide triplets. An abasic nucleotide resembles a pre-formed RAD51 binding site, making the binding process energetically favorable. This is evidenced by the faster association with a DNA molecule containing even a single AP site. The ability to recognize AP sites suggests that these lesions are the likely preferred nucleation points for RAD51 polymerization on DNA.

Cryo-EM demonstrates RAD51's unique ability to selectively bind abasic DNA, assembling specifically on strands with AP sites in dsDNA. RAD51's selective binding to AP sites, independently of ssDNA gaps, is confirmed by increased recruitment to geminin-treated chromatin containing non-replicating abasic dsDNA.

The similarity in DNA recognition between RAD51 and its orthologs, including bacterial RecA,[53,54] suggests that AP-site recognition might be a conserved trait, predating complex HR processes like strand pairing and homology searching. These results align with RecA's role in preventing DNA degradation by the UvrABC complex,[55] which can process DNA with AP sites.[56] As AP sites are a fundamental DNA vulnerability,[1] RAD51's protection of abasic DNA may represent a primordial function of this protein family.

RAD51-mediated protection of abasic DNA from nucleases

RAD51's enhanced binding kinetics to abasic DNA is critical to protect AP sites from enzymatic processing possibly by outcompeting nucleases, thus preventing AP-site cleavage (Figure 7A). Among these, MRE11, a prominent S-phase nuclease,[14,57–59] can cleave AP sites.[34] However, RAD51 effectively shields AP sites during replication, averting fork collapse. This protection persists until polymerases such as POLθ and possibly other TLS enzymes intervene to bypass the lesion and fill the gap induced by AP-site stalling nascent DNA synthesis (Figure 7A). POLθ's ability to displace RAD51 might facilitate this task.[60]

EM analysis of replication intermediates with uneven fork branches[15] shows that without RAD51, breakages mainly occur in areas with ssDNA gaps (Figure 7B).

Unlike RAD51, the RPA ssDNA binding protein complex may be less effective at preventing ssDNA cleavage by AP endonucleases. This is due to its dynamic binding to ssDNA[61,62] that could briefly expose ssDNA to nucleases and glycosylases.[61] In contrast, RAD51 stably encapsulates DNA within its NPF structure, shielding it from external access. A role for stable NPFs in protecting against different nucleases is consistent with BRCA2/RAD51's ability to suppress nascent DNA degradation at reversed replication forks[63] and ssDNA gaps,[14] preventing extensive formation of ssDNA regions on replication intermediates.[14,15,32]

Overall, our findings highlight the unique RAD51's function in safeguarding replicating DNA templates with AP sites from breaking. This role differs from the repair of DSBs possibly resulting from AP sites originating from nascent DNA misincorporation of BER substrates, including 5hmdU generated by cytoplasmic deaminases, that compromises the survival of cells with impaired DSB repair.[11,12]

Considering APE1's preference for dsDNA[64] and our observations of increased γH2AX foci in APEX1^{−/−} cells after BRCA2 or RAD51 silencing, it is unlikely that APE1 significantly contributes to replication forks cleavage. However, RAD51 may prevent excessive nicking by APE1 at loci undergoing BER-mediated events leading to AP sites' formation in dsDNA ahead of replication forks, thus preventing DSBs occurrence at fork passage.

Figure 5. Replicative, abasic ssDNA gap accumulation in repair-defective human cancer cells

(A) Schematic of APE1 and S1 nuclease cleavage of abasic DNA causing DSBs.

(B) Scatter dot plot of IdU track lengths on the indicated number of DNA fibers from DLD1 WT cells treated with DMSO or APE1i, post S1 or APE1 treatment. Horizontal bars indicate mean ± SD of all data points from independent experiments. Overlay dots show n = 3 independent biological replicate means. Kruskal-Wallis test, followed by Dunn's post hoc test for multiple comparisons; **$p < 0.01$; ***$p < 0.001$; ****$p < 0.0001$; ns, non-significant.

(C) ELISA-based AP-site quantification in DNA from WT, BRCA2^{−/−}, or APEX1^{−/−} DLD1 cells. Horizontal bars indicate mean ± SD of all data points. Dots show n = 3 independent biological replicate means. One-way ANOVA, followed by Dunnett's post hoc test; *$p < 0.05$.

(D) AP sites quantification in the indicated number of WT, BRCA2^{−/−}, or APEX1^{−/−} DLD1 cells using Alexa Fluor 647-AA3. Bars indicate mean ± SD of all data points. Dots show n = 3 independent biological replicate medians. Boxes indicate interquartile with ranges. One-way ANOVA, followed by Dunnett's post hoc test; **$p < 0.01$.

(E) Representative images of DLD1 WT, APEX1^{−/−}, BRCA2^{−/−} nuclei with Alexa 647-AA3. Scale bars, 10 μm.

(F) IdU track lengths on the indicated numbers of DNA fibers from DLD1 WT, APEX1^{−/−}, BRCA2^{−/−} cells, post buffer, S1, or APE1 treatment. Bars indicate mean ± SD of all data points. Overlay dots show n = 2 independent biological replicate medians. Kruskal-Wallis test, followed by Dunn's post hoc test; ****$p < 0.0001$; ns, non-significant.

(G) Similar to (F), on fibers derived from cells treated with control or SMUG1 siRNAs. Bars indicate mean ± SD of all data points. Overlay dots show n = 3 independent biological replicate medians. Kruskal-Wallis test, followed by Dunn's post hoc test; ***$p < 0.0001$****$p < 0.0001$; ns, non-significant.

(H) Denaturing gel showing fluorescein-ssDNA with uracil incubated with RAD51, then xSMUG1, and boiled before xAPE1 treatment.

(I and J) (I) IdU track lengths on the indicated number of fibers from DNMT1[NA] and (J) DNMT1[NA]/DNMT3B^{−/−} DLD1 cells following treatment with control or BRCA2 siRNAs and DMSO or IAA. Cells were treated with S1 or APE1. Bars indicate mean ± SD of all data points. Overlay dots show n = 3 independent biological replicate medians. Kruskal-Wallis test, followed by Dunn's post hoc test; ****$p < 0.0001$; ns, non-significant.

(K) IdU track lengths on the indicated number fibers from DLD1 BRCA2^{−/−} cells treated with control or TET2 siRNAs, post S1, or APE1 treatment. Bars indicate mean ± SD of all data points. Overlay dots show n = 3 independent biological replicate medians. Kruskal-Wallis, followed by Dunn's post hoc test; ****$p < 0.0001$; ns, non-significant.
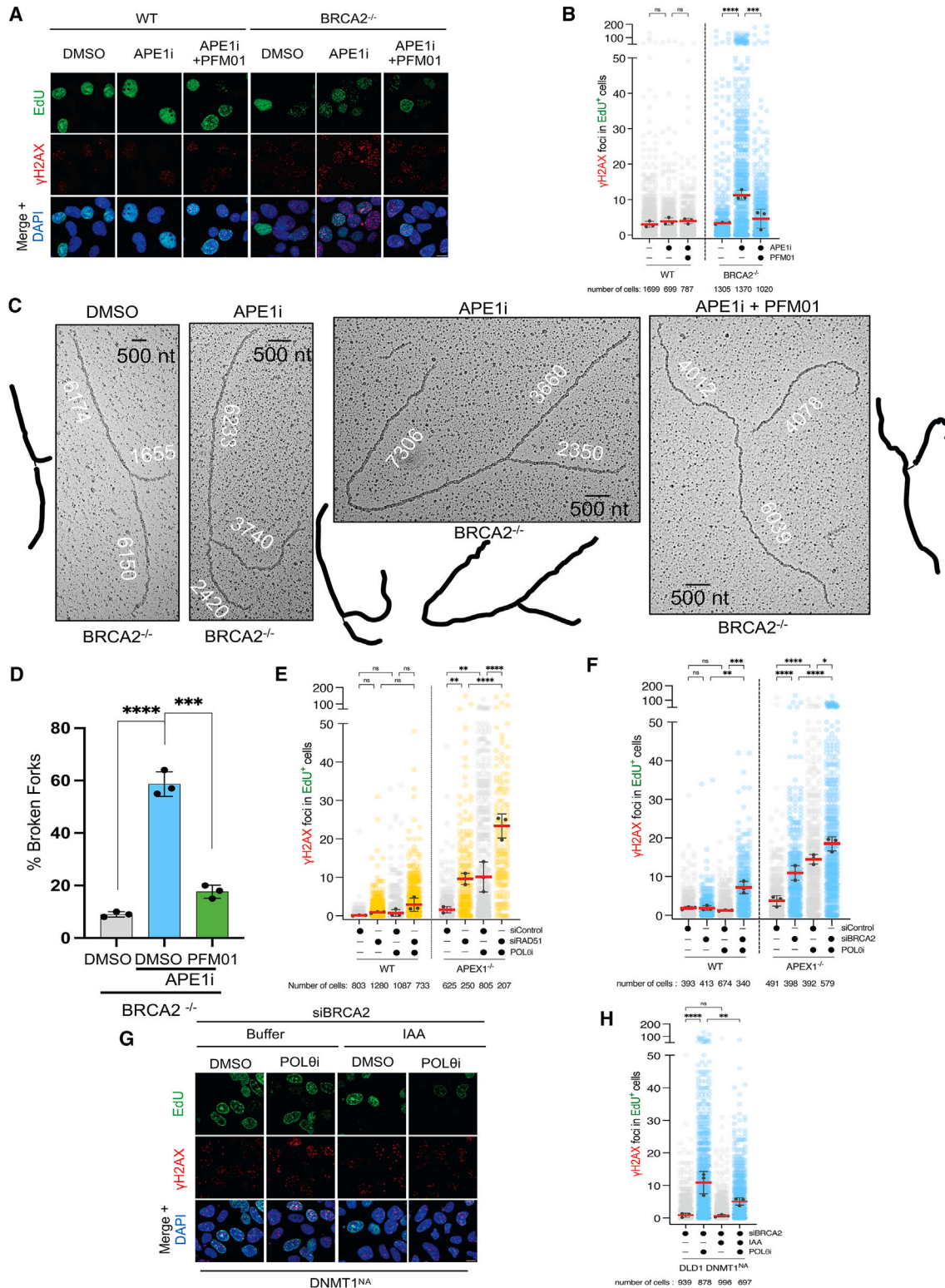
See also Figures S5–S7.

Figure 6. BRCA2- and RAD51-mediated suppression of MRE11-mediated fork breakage

(A) Images of γH2AX foci in EdU-labeled DLD1 WT and BRCA2$^{-/-}$ cells post-treatment with DMSO, APE1i or APE1i and PFM01.

(B) Quantification of γH2AX foci in the indicated number of cells. Bars indicate mean ± SD of all data points. Overlay dots indicate $n = 3$ independent biological replicate means. One-way ANOVA, followed by Tukey's post hoc test for multiple comparisons; **$p < 0.01$; ***$p < 0.001$; ****$p < 0.0001$; ns, non-significant.

(legend continued on next page)

RAD51-mediated control of AP sites and abasic ssDNA gap accumulation

To study the impact of RAD51 on abasic DNA templates undergoing replication, we developed an assay based on APE1-mediated cleavage of replicating DNA fibers. Abasic template cleavage by APE1 leads to the shortening of the labeled DNA fiber only when occurring in the context of a ssDNA gap. This assay can therefore clearly distinguish AP sites present in the replicating template from the ones occurring within nascent DNA or un-replicated dsDNA ahead of the replication forks.

Using the APE1-fiber assay, we demonstrate that in the absence of BRCA2, which is required for the loading and the stabilization of RAD51 NPFs onto replicating DNA,[65,66] AP-site containing ssDNA gaps accumulate during DNA replication.

These results together with the overall AP increase measured in BRCA2-defective cells provide evidence that RAD51 not only shields AP sites from nuclease activity but also suppresses their accumulation. RAD51 trailing behind forks or nucleating at AP sites and spreading laterally could restrict the unfettered activity of enzymes that contribute to the formation of AP sites on exposed ssDNA strands. These enzymes include glycosylases and deaminases acting on ssDNA[3–6,67] (Figure 7C). This function could be important to prevent widespread base changes observed in HR-defective cells.[68] The similarity between *Xl* and human cells indicates RAD51's conserved role in managing AP sites across species.

The requirement for stable RAD51 NPFs to prevent DNA access of AP sites inducing enzymes may explain ssDNA gap formation in murine cells with the mouse equivalent of the BRCA2[S3291A] mutation,[69] a base substitution that only minimally affects human BRCA2-mediated stabilization of RAD51 NPFs, as recently noted.[66] Efficient formation of NPFs nucleating from AP sites might be required to prevent glycosylase access to adjacent ssDNA regions and restrain further abasic sites and gaps accumulation.

The rapid delivery of RAD51 to abasic DNA necessary to outcompete cleavage by AP site-specific nucleases might be instead compromised by more severe BRCA2 mutations that also impact HR and cellular viability upon DNA damage.[69]

The suppression of AP sites' accumulation by BRCA2/RAD51 might not be confined to ssDNA but could extend to dsDNA regions, including enhancers, which preferentially bind RAD51[70] and are subjected to TDG-dependent DNA demethylation,[71] preventing further DNA damage.

Compensatory mechanisms preventing deleterious consequences of AP sites' formation in the absence of BRCA2 or RAD51

In HR-defective cells, alternative pathways can partially compensate for the absence of abasic DNA protection. One such pathway relies on POLθ's ability to replicate across AP sites,[36] by filling in the ssDNA gaps created by PRIMPOL repriming downstream of the AP lesion on the leading strand or arising in between stalled Okazaki fragments, which would be normally protected by BRCA2/RAD51.[15] Abasic gap filling would contribute to explain the synthetic lethality induced by POLθ polymerase inhibitors in unchallenged BRCA2-defective cells in addition to the established POLθ's role in DSB repair.[15,21,72]

Additional protection is conferred by HMCES shielding AP sites,[28] and by TLS polymerases, which can also bypass AP sites,[73] serving as a backup pathway in HR-defective cells[13,74] or cells that overexpress APOBEC3 enzymes.[38,75] The interplay among POLθ and TLS polymerases, including Pol ζ, is likely to be additive[15,21] and highly regulated as already shown for HMCES, which restricts TLS polymerases engagement with replicating DNA.[38] The expression levels of these factors might impact on the number, the size and the fate of abasic ssDNA gaps.

Origins of AP sites impacting DNA replication

Unexpectedly, DNMT1-dependent 5mdC production is a prerequisite for replicative abasic ssDNA gaps' accumulation and DSBs' formation in the absence of BRCA2/RAD51- and POLθ-mediated gap filling.

Physiological turnover of 5mdC is regulated by the TET enzymes, which oxidize 5mdC to 5hmdC and then 5fdC and 5cadC. These forms are removed by BER through TDG in the context of dsDNA to replace modified cytosines with unmodified ones[3] (Figure 7D).

In contrast to TET2 downregulation, TDG silencing does not prevent abasic ssDNA gap formation in BRCA2^{−/−} cells, suggesting that TDG-mediated 5mdC demethylation is not involved in replicative ssDNA gap formation, consistent TDG expression outside S-phase.[3] However, we cannot exclude that a fraction of AP sites accumulating in the absence of BRCA2 is still contributed by TDG activity beyond S-phase.

Once generated, 5hmdC can be deaminated to yield 5hmdU, which is then processed by SMUG1 within ssDNA[4,5,46] (Figure 7C).

APOBEC3 and AID deaminases promote widespread cancer genome mutagenesis.[76] In particular, APOBEC3B, APOBEC3C, and APOBEC3D can be found expressed in multiple

---

(C) EM of replication forks from BRCA2^{−/−} DLD1 cells treated with DMSO, APE1i, or APE1i and PFM01.

(D) Percentage of broken forks from extracts treated as indicated. Bars indicate mean ± SD relative to a total of 72 forks. Overlay dots show $n = 3$ independent biological replicate means. One-way ANOVA, followed by Dunnet's post hoc test; ****$p < 0.0001$.

(E and F) (E) Quantification of γH2AX foci in the indicated number of DLD1 cells treated with control, RAD51 or (F) BRCA2 siRNAs. Bars indicate mean ± SD of all data points. Overlay dots indicate $n = 3$ independent experiment means. One-way ANOVA, followed by Tukey's post hoc test; **$p < 0.01$; ***$p < 0.001$; ****$p < 0.0001$; ns, non-significant.

(G) Images of γH2AX foci in EdU-labeled DNMT1[NA] DLD1 cells treated with BRCA2 siRNAs, followed by DMSO or 5 μM POLθi. Buffer or IAA were supplemented where indicated.

(H) Quantification of γH2AX foci shown in (G). Horizontal bars indicate mean ± SD of all data points. Overlay dots indicate independent biological replicate means. $n = 3$; one-way ANOVA, followed by Tukey's post hoc test; **$p < 0.01$; ****$p < 0.0001$; ns, non-significant.
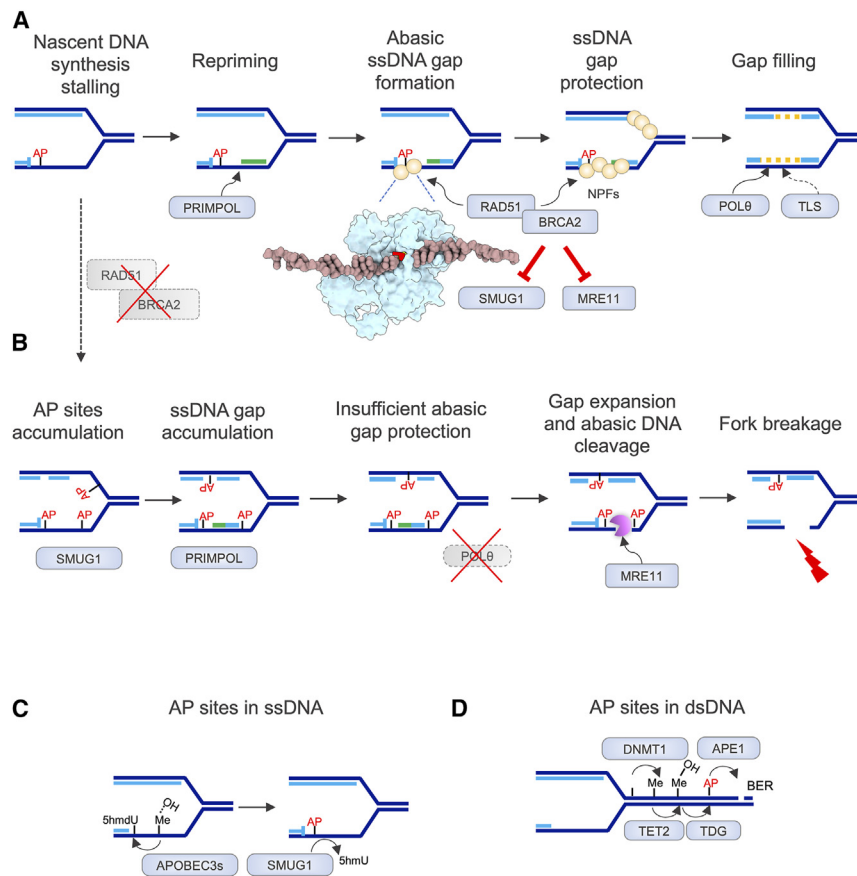
See also Figures S5–S7.

Figure 7. Model for BRCA2- and RAD51-mediated protection against AP site-induced fork breakage

(A) Unrepaired AP sites stall nascent DNA synthesis. Restart by PRIMPOL leads to ssDNA gaps. RAD51 binds to unrepaired AP sites. Stabilized by BRCA2, RAD51 NPFs suppress AP sites cleavage by MRE11 and restrict further SMUG1 driven AP-site accumulation. Gap sealing is facilitated by POLθ and, possibly, TLS polymerases bypassing AP sites.

(B) Without BRCA2/RAD51, unrestricted SMUG1 access to ssDNA promotes AP sites and abasic gap accumulation. MRE11 extends ssDNA gaps and cleaves unprotected AP sites within ssDNA, especially in the absence of POLθ, causing replication fork breakage.

(C) APOBEC3B-dependent deamination of 5hmdC or 5mdC leads to transient 5hmdU formation, directly or indirectly. SMUG1 mediated removal of 5hmU promotes AP sites accumulation in ssDNA.

(D) TET2-dependent hydroxylation of 5mdC followed by TDG-mediated removal of the 5hmdC derivatives promotes the formation of AP sites in dsDNA repaired by BER.

tumors, especially following DNA damage.[47–49] Accordingly, APOBEC3C and APOBEC3D have been recently shown to promote RAD51 loading onto replicating DNA in the absence of DSBs.[48]

5hmdU is likely to be short lived due to its rapid formation and removal from ssDNA templates during DNA replication. This might explain the low levels of 5hmdU measured in total genomic DNA.[77]

5hmdU formation might be stimulated by TET2-dependent accumulation of 5hmdC at under-replicated and damaged DNA[78] occurring in HR-defective backgrounds.[79,80]

Alternatively, 5hmdU could indirectly arise from APOBEC3-dependent deamination of 5mdC to yield 5mdU (dT), which can be oxidized to 5hmdU by TET2.[77] These events might take place in regions of high TET2 activity[81] coupled to APOBEC3s enzymes. The complete characterization of the enzymatic events leading to AP sites from 5mdC awaits further clarification of these pathways.

Intriguingly, concurrent evolution of HR genes and appearance of DNA methylation in higher eukaryotes has been reported.[82]

Overall, we established a direct connection between RAD51 and the protection of unrepaired AP sites from unregulated cleavage leading to fork breakage. In line with our findings, high levels of RAD51, commonly found in cancer cells[83] confer therapy resistance without completely restoring recombination in HR-defective cells.[84] Molecules targeting RAD51's ability to protect AP sites might be designed to overcome resistance to therapy in RAD51 overexpressing cancer cells.

Limitations of the study

We could not find mutations in RAD51 that selectively eliminate its recognition of AP sites without also affecting RAD51's DNA-binding ability in the NPF as the DNA binding and interaction with AP sites depend on the same L1-L2 domains and residues in RAD51. Additionally, a possible role of RAD51 in repairing AP sites has not been defined yet.

STAR★METHODS

Detailed methods are provided in the online version of this paper and include the following:

- KEY RESOURCES TABLE
- RESOURCE AVAILABILITY
  - Lead contact
  - Materials availability
  - Data and code availability
- EXPERIMENTAL MODEL AND STUDY PARTICIPANT DETAILS
  - *Xenopus laevis* eggs
  - Cell lines and culture
  - Generation of DLD1 APEX1 knockout cell line
  - Generation of DLD1 DNMT1^{NA} and DNMT1^{NA} DNMT3B$^{-/-}$ cell lines
- METHOD DETAILS
  - Expression and purification of recombinant proteins
  - Cloning
  - DNA oligonucleotides for EMSA, SPR, and Cryo-EM
  - Electrophoretic mobility shift assays (EMSA)
  - Surface plasmon resonance (SPR)
  - Vitrification of RAD51 filament grids
  - CryoEM data collection and processing

- ○ Real-space refinement
- ○ Egg extract and chromatin binding
- ○ *In vitro* enzymatic assays with DNA oligos
- ○ DNA electron microscopy
- ○ Chemical reagents
- ○ Antibodies
- ○ RNA interference
- ○ Cell viability assays
- ○ AP site quantification
- ○ Western blotting
- ○ Cell immunofluorescence
- ○ DNA fiber assay with S1 nuclease
- ○ DNA fiber assay with APE1 nuclease
- ● QUANTIFICATION AND STATISTICAL ANALYSIS
  - ○ Statistical analysis

SUPPLEMENTAL INFORMATION

Supplemental information can be found online at https://doi.org/10.1016/j.molcel.2024.07.004.

ACKNOWLEDGMENTS

AUTHOR CONTRIBUTIONS

Y.W.H., M.A.R.-O., R.A., A.D.A., L.J., V.S., S.W., and A.A. performed all the experiments and analyzed the data. V.B. and D.F. produced the DNMTs cell lines and edited the manuscript. L.P. and V.C. analyzed the data, supervised the experiments, and wrote the manuscript. L.P. and V.C. are both corresponding authors as responsible for relevant complementary aspects of the work represented by structural and functional analysis, respectively. All authors agree that the contributions of M.A.R.-O., Y.W.H., and R.A are equal and that their positions on the author list can be swapped around on CVs, websites, and elsewhere if desired.

DECLARATION OF INTERESTS

The authors confirm that there are no relevant financial or nonfinancial competing interests to report.

REFERENCES

1. Lindahl, T. (1993). Instability and decay of the primary structure of DNA. Nature *362*, 709–715. https://doi.org/10.1038/362709a0.

2. Caldecott, K.W. (2020). Mammalian DNA base excision repair: Dancing in the moonlight. DNA Repair *93*, 102921. https://doi.org/10.1016/j.dnarep.2020.102921.

3. Kohli, R.M., and Zhang, Y. (2013). TET enzymes, TDG and the dynamics of DNA demethylation. Nature *502*, 472–479. https://doi.org/10.1038/nature12750.

4. Haushalter, K.A., Todd Stukenberg, M.W., Kirschner, M.W., and Verdine, G.L. (1999). Identification of a new uracil-DNA glycosylase family by expression cloning using synthetic inhibitors. Curr. Biol. *9*, 174–185. https://doi.org/10.1016/s0960-9822(99)80087-6.

5. Krokan, H.E., Drabløs, F., and Slupphaug, G. (2002). Uracil in DNA–occurrence, consequences and repair. Oncogene *21*, 8935–8948. https://doi.org/10.1038/sj.onc.1205996.

6. Olinski, R., Starczak, M., and Gackowski, D. (2016). Enigmatic 5-hydroxymethyluracil: Oxidatively modified base, epigenetic mark or both? Mutat. Res. Rev. Mutat. Res. *767*, 59–66. https://doi.org/10.1016/j.mrrev.2016.02.00.

7. González-Prieto, R., Muñoz-Cabello, A.M., Cabello-Lobato, M.J., and Prado, F. (2013). Rad51 replication fork recruitment is required for DNA damage tolerance. EMBO J. *32*, 1307–1321. https://doi.org/10.1038/emboj.2013.73.

8. Mengwasser, K.E., Adeyemi, R.O., Leng, Y., Choi, M.Y., Clairmont, C., D'Andrea, A.D., and Elledge, S.J. (2019). Genetic Screens Reveal FEN1 and APEX2 as BRCA2 Synthetic Lethal Targets. Mol. Cell *73*, 885–899.e6. https://doi.org/10.1016/j.molcel.2018.12.008.

9. Serrano-Benitez, A., Wells, S.E., Drummond-Clarke, L., Russo, L.C., Thomas, J.C., Leal, G.A., Farrow, M., Edgerton, J.M., Balasubramanian, S., Yang, M., et al. (2023). Unrepaired base excision repair intermediates in template DNA strands trigger replication fork collapse and PARP inhibitor sensitivity. EMBO J. *42*, e113190. https://doi.org/10.15252/embj.2022113190.

10. Kharat, S.S., Ding, X., Swaminathan, D., Suresh, A., Singh, M., Sengodan, S.K., Burkett, S., Marks, H., Pamala, C., He, Y., et al. (2020). Degradation of 5hmC-marked stalled replication forks by APE1 causes genomic instability. Sci. Signal. *13*, eaba8091. https://doi.org/10.1126/scisignal.aba8091.

11. Fugger, K., Bajrami, I., Silva Dos Santos, M., Young, S.J., Kunzelmann, S., Kelly, G., Hewitt, G., Patel, H., Goldstone, R., Carell, T., et al. (2021). Targeting the nucleotide salvage factor DNPH1 sensitizes BRCA-deficient cells to PARP inhibitors. Science *372*, 156–165. https://doi.org/10.1126/science.abb4542.

12. Peña-Gómez, M.J., Moreno-Gordillo, P., Narmontė, M., García-Calderón, C.B., Rukšėnaitė, A., Klimašauskas, S., and Rosado, I.V. (2022). FANCD2 maintains replication fork stability during misincorporation of the DNA demethylation products 5-hydroxymethyl-2′-deoxycytidine and 5-hydroxymethyl-2′-deoxyuridine. Cell Death Dis. *13*, 503. https://doi.org/10.1038/s41419-022-04952-0.

13. Taglialatela, A., Leuzzi, G., Sannino, V., Cuella-Martin, R., Huang, J.W., Wu-Baer, F., Baer, R., Costanzo, V., and Ciccia, A. (2021). REV1-Polzeta maintains the viability of homologous recombination-deficient cancer cells through mutagenic repair of PRIMPOL-dependent ssDNA gaps. Mol. Cell *81*, 4008–4025.e7. https://doi.org/10.1016/j.molcel.2021.08.016.

14. Hashimoto, Y., Ray Chaudhuri, A., Lopes, M., and Costanzo, V. (2010). Rad51 protects nascent DNA from Mre11-dependent degradation and promotes continuous DNA synthesis. Nat. Struct. Mol. Biol. *17*, 1305–1311. https://doi.org/10.1038/nsmb.1927.

15. Mann, A., Ramirez-Otero, M.A., De Antoni, A., Hanthi, Y.W., Sannino, V., Baldi, G., Falbo, L., Schrempf, A., Bernardo, S., Loizou, J., and Costanzo, V. (2022). POLtheta prevents MRE11-NBS1-CtIP-dependent fork breakage in the absence of BRCA2/RAD51 by filling lagging-strand gaps. Mol. Cell *82*, 4218–4231.e8. https://doi.org/10.1016/j.molcel.2022.09.013.

16. Cantor, S.B. (2021). Revisiting the BRCA-pathway through the lens of replication gap suppression: "Gaps determine therapy response in

BRCA mutant cancer". DNA Repair *107*, 103209. https://doi.org/10.1016/j.dnarep.2021.103209.

17. Cong, K., Peng, M., Kousholt, A.N., Lee, W.T.C., Lee, S., Nayak, S., Krais, J., VanderVere-Carozza, P.S., Pawelczak, K.S., Calvo, J., et al. (2021). Replication gaps are a key determinant of PARP inhibitor synthetic lethality with BRCA deficiency. Mol. Cell *81*, 3128–3144.e7. https://doi.org/10.1016/j.molcel.2021.06.011.

18. Feng, W., and Jasin, M. (2017). BRCA2 suppresses replication stress-induced mitotic and G1 abnormalities through homologous recombination. Nat. Commun. *8*, 525. https://doi.org/10.1038/s41467-017-00634-0.

19. Quinet, A., Tirman, S., Jackson, J., Šviković, S., Lemaçon, D., Carvajal-Maldonado, D., González-Acosta, D., Vessoni, A.T., Cybulla, E., Wood, M., et al. (2020). PRIMPOL-Mediated Adaptive Response Suppresses Replication Fork Reversal in BRCA-Deficient Cells. Mol. Cell *77*, 461–474.e9. https://doi.org/10.1016/j.molcel.2019.10.008.

20. Tirman, S., Quinet, A., Wood, M., Meroni, A., Cybulla, E., Jackson, J., Pegoraro, S., Simoneau, A., Zou, L., and Vindigni, A. (2021). Temporally distinct post-replicative repair mechanisms fill PRIMPOL-dependent ssDNA gaps in human cells. Mol. Cell *81*, 4026–4040.e8. https://doi.org/10.1016/j.molcel.2021.09.013.

21. Schrempf, A., Bernardo, S., Arasa Verge, E.A., Ramirez Otero, M.A., Wilson, J., Kirchhofer, D., Timelthaler, G., Ambros, A.M., Kaya, A., Wieder, M., et al. (2022). POLtheta processes ssDNA gaps and promotes replication fork progression in BRCA1-deficient cells. Cell Rep. *41*, 111716. https://doi.org/10.1016/j.celrep.2022.111716.

22. Xu, J., Zhao, L., Xu, Y., Zhao, W., Sung, P., and Wang, H.W. (2017). Cryo-EM structures of human RAD51 recombinase filaments during catalysis of DNA-strand exchange. Nat. Struct. Mol. Biol. *24*, 40–46. https://doi.org/10.1038/nsmb.3336.

23. Appleby, R., Bollschweiler, D., Chirgadze, D.Y., Joudeh, L., and Pellegrini, L. (2023). A metal ion-dependent mechanism of RAD51 nucleoprotein filament disassembly. iScience *26*, 106689. https://doi.org/10.1016/j.isci.2023.106689.

24. Chen, V.B., Arendall, W.B., 3rd, Headd, J.J., Keedy, D.A., Immormino, R.M., Kapral, G.J., Murray, L.W., Richardson, J.S., and Richardson, D.C. (2010). MolProbity: all-atom structure validation for macromolecular crystallography. Acta Crystallogr. D Biol. Crystallogr. *66*, 12–21. https://doi.org/10.1107/S0907444909042073.

25. Afonine, P.V., Klaholz, B.P., Moriarty, N.W., Poon, B.K., Sobolev, O.V., Terwilliger, T.C., Adams, P.D., and Urzhumtsev, A. (2018). New tools for the analysis and validation of cryo-EM maps and atomic models. Acta Crystallogr. D Struct. Biol. *74*, 814–840. https://doi.org/10.1107/S2059798318009324.

26. Wilson, D.M., 3rd, and Simeonov, A. (2010). Small molecule inhibitors of DNA repair nuclease activities of APE1. Cell. Mol. Life Sci. *67*, 3621–3631. https://doi.org/10.1007/s00018-010-0488-2.

27. Rai, G., Vyjayanti, V.N., Dorjsuren, D., Simeonov, A., Jadhav, A., Wilson, D.M., 3rd, and Maloney, D.J. (2012). Synthesis, biological evaluation, and structure-activity relationships of a novel class of apurinic/apyrimidinic endonuclease 1 inhibitors. J. Med. Chem. *55*, 3101–3112. https://doi.org/10.1021/jm201537d.

28. Mohni, K.N., Wessel, S.R., Zhao, R., Wojciechowski, A.C., Luzwick, J.W., Layden, H., Eichman, B.F., Thompson, P.S., Mehta, K.P.M., and Cortez, D. (2019). HMCES Maintains Genome Integrity by Shielding Abasic Sites in Single-Strand DNA. Cell *176*, 144–153.e13. https://doi.org/10.1016/j.cell.2018.10.055.

29. Ide, H., Akamatsu, K., Kimura, Y., Michiue, K., Makino, K., Asaeda, A., Takamori, Y., and Kubo, K. (1993). Synthesis and damage specificity of a novel probe for the detection of abasic sites in DNA. Biochemistry *32*, 8276–8283. https://doi.org/10.1021/bi00083a031.

30. Raja, S., and Van Houten, B. (2021). The Multiple Cellular Roles of SMUG1 in Genome Maintenance and Cancer. Int. J. Mol. Sci. *22*, 1981. https://doi.org/10.3390/ijms22041981.

31. McGarry, T.J., and Kirschner, M.W. (1998). Geminin, an inhibitor of DNA replication, is degraded during mitosis. Cell *93*, 1043–1053. https://doi.org/10.1016/s0092-8674(00)81209-x.

32. Kolinjivadi, A.M., Sannino, V., De Antoni, A., Zadorozhny, K., Kilkenny, M., Técher, H., Baldi, G., Shen, R., Ciccia, A., Pellegrini, L., et al. (2017). Smarcal1-Mediated Fork Reversal Triggers Mre11-Dependent Degradation of Nascent DNA in the Absence of Brca2 and Stable Rad51 Nucleofilaments. Mol. Cell *67*, 867–881.e7. https://doi.org/10.1016/j.molcel.2017.07.001.

33. Bhaskara, V., Dupré, A., Lengsfeld, B., Hopkins, B.B., Chan, A., Lee, J.H., Zhang, X., Gautier, J., Zakian, V., and Paull, T.T. (2007). Rad50 adenylate kinase activity regulates DNA tethering by Mre11/Rad50 complexes. Mol. Cell *25*, 647–661. https://doi.org/10.1016/j.molcel.2007.01.028.

34. Larson, E.D., Cummings, W.J., Bednarski, D.W., and Maizels, N. (2005). MRE11/RAD50 cleaves DNA in the AID/UNG-dependent pathway of immunoglobulin gene diversification. Mol. Cell *20*, 367–375. https://doi.org/10.1016/j.molcel.2005.09.018.

35. Moiani, D., Ronato, D.A., Brosey, C.A., Arvai, A.S., Syed, A., Masson, J.Y., Petricci, E., and Tainer, J.A. (2018). Targeting Allostery with Avatars to Design Inhibitors Assessed by Cell Activity: Dissecting MRE11 Endo- and Exonuclease Activities. Methods Enzymol. *601*, 205–241. https://doi.org/10.1016/bs.mie.2017.11.030.

36. Seki, M., Masutani, C., Yang, L.W., Schuffert, A., Iwai, S., Bahar, I., and Wood, R.D. (2004). High-efficiency bypass of DNA damage by human DNA polymerase Q. EMBO J. *23*, 4484–4494. https://doi.org/10.1038/sj.emboj.7600424.

37. Quinet, A., Carvajal-Maldonado, D., Lemacon, D., and Vindigni, A. (2017). DNA Fiber Analysis: Mind the Gap! Methods Enzymol. *591*, 55–82. https://doi.org/10.1016/bs.mie.2017.03.019.

38. Mehta, K.P.M., Lovejoy, C.A., Zhao, R., Heintzman, D.R., and Cortez, D. (2020). HMCES Maintains Replication Fork Progression and Prevents Double-Strand Breaks in Response to APOBEC Deamination and Abasic Site Formation. Cell Rep. *31*, 107705. https://doi.org/10.1016/j.celrep.2020.107705.

39. Wei, S., Shalhout, S., Ahn, Y.H., and Bhagwat, A.S. (2015). A versatile new tool to quantify abasic sites in DNA and inhibit base excision repair. DNA Repair *27*, 9–18. https://doi.org/10.1016/j.dnarep.2014.12.006.

40. Cai, Y., Cao, H., Wang, F., Zhang, Y., and Kapranov, P. (2022). Complex genomic patterns of abasic sites in mammalian DNA revealed by a high-resolution SSiNGLe-AP method. Nat. Commun. *13*, 5868. https://doi.org/10.1038/s41467-022-33594-1.

41. Panzarino, N.J., Krais, J.J., Cong, K., Peng, M., Mosqueda, M., Nayak, S.U., Bond, S.M., Calvo, J.A., Doshi, M.B., Bere, M., et al. (2021). Replication Gaps Underlie BRCA-deficiency and Therapy Response. Cancer Res. *81*, 1388–1397. https://doi.org/10.1158/0008-5472.CAN-20-1602.

42. Sakai, W., Swisher, E.M., Jacquemont, C., Chandramohan, K.V., Couch, F.J., Langdon, S.P., Wurz, K., Higgins, J., Villegas, E., and Taniguchi, T. (2009). Functional restoration of BRCA2 protein by secondary BRCA2 mutations in BRCA2-mutated ovarian carcinoma. Cancer Res. *69*, 6381–6386. https://doi.org/10.1158/0008-5472.CAN-09-1178.

43. Gowher, H., and Jeltsch, A. (2018). Mammalian DNA methyltransferases: new discoveries and open questions. Biochem. Soc. Trans. *46*, 1191–1202. https://doi.org/10.1042/BST20170574.

44. Nishimura, K., Fukagawa, T., Takisawa, H., Kakimoto, T., and Kanemaki, M. (2009). An auxin-based degron system for the rapid depletion of proteins in nonplant cells. Nat. Methods *6*, 917–922. https://doi.org/10.1038/nmeth.1401.

45. Scelfo, A., Barra, V., Abdennur, N., Spracklin, G., Busato, F., Salinas-Luypaert, C., Bonaiti, E., Velasco, G., Bonhomme, F., Chipont, A., et al. (2024). Tunable DNMT1 degradation reveals DNMT1/DNMT3B synergy in DNA methylation and genome organization. J. Cell Biol. *223*, e202307026. https://doi.org/10.1083/jcb.202307026.

46. Schutsky, E.K., Nabel, C.S., Davis, A.K.F., DeNizio, J.E., and Kohli, R.M. (2017). APOBEC3A efficiently deaminates methylated, but not TET-oxidized, cytosine bases in DNA. Nucleic Acids Res. *45*, 7655–7665. https://doi.org/10.1093/nar/gkx345.

47. Burns, M.B., Temiz, N.A., and Harris, R.S. (2013). Evidence for APOBEC3B mutagenesis in multiple human cancers. Nat. Genet. *45*, 977–983. https://doi.org/10.1038/ng.2701.

48. Ubhi, T., Zaslaver, O., Quaile, A.T., Plenker, D., Cao, P., Pham, N.A., Békési, A., Jang, G.H., O'Kane, G.M., Notta, F., et al. (2024). Cytidine deaminases APOBEC3C and APOBEC3D promote DNA replication stress resistance in pancreatic cancer cells. Nat. Cancer *5*, 895–915. https://doi.org/10.1038/s43018-024-00742-z.

49. Pecori, R., Di Giorgio, S., Paulo Lorenzo, J., and Nina Papavasiliou, F. (2022). Functions and consequences of AID/APOBEC-mediated DNA and RNA deamination. Nat. Rev. Genet. *23*, 505–518. https://doi.org/10.1038/s41576-022-00459-8.

50. Ghandi, M., Huang, F.W., Jané-Valbuena, J., Kryukov, G.V., Lo, C.C., McDonald, E.R., 3rd, Barretina, J., Gelfand, E.T., Bielski, C.M., Li, H., et al. (2019). Next-generation characterization of the Cancer Cell Line Encyclopedia. Nature *569*, 503–508. https://doi.org/10.1038/s41586-019-1186-3.

51. Heyer, W.D. (2007). Biochemistry of eukaryotic homologous recombination. Top. Curr. Genet. *17*, 95–133. https://doi.org/10.1007/978-3-540-71021-9.

52. Symington, L.S., and Gautier, J. (2011). Double-strand break end resection and repair pathway choice. Annu. Rev. Genet. *45*, 247–271. https://doi.org/10.1146/annurev-genet-110410-132435.

53. West, S.C. (2003). Molecular views of recombination proteins and their control. Nat. Rev. Mol. Cell Biol. *4*, 435–445. https://doi.org/10.1038/nrm1127.

54. Chen, Z., Yang, H., and Pavletich, N.P. (2008). Mechanism of homologous recombination from the RecA-ssDNA/dsDNA structures. Nature *453*, 489–494. https://doi.org/10.1038/nature06971.

55. Horii, Z.I., and Suzuki, K. (1970). Degradation of the DNA of recA mutants of Escherichia coli K-12 after irradiation with ultraviolet light. II. Further studies including a recA uvrA double mutant. Photochem. Photobiol. *11*, 99–107. https://doi.org/10.1111/j.1751-1097.1970.tb05976.x.

56. Snowden, A., Kow, Y.W., and Van Houten, B. (1990). Damage repertoire of the Escherichia coli UvrABC nuclease complex includes abasic sites, base-damage analogues, and lesions containing adjacent 5′ or 3′ nicks. Biochemistry *29*, 7251–7259. https://doi.org/10.1021/bi00483a013.

57. Haber, J.E. (1998). The many interfaces of Mre11. Cell *95*, 583–586. https://doi.org/10.1016/s0092-8674(00)81626-8.

58. Syed, A., and Tainer, J.A. (2018). The MRE11-RAD50-NBS1 Complex Conducts the Orchestration of Damage Signaling and Outcomes to Stress in DNA Replication and Repair. Annu. Rev. Biochem. *87*, 263–294. https://doi.org/10.1146/annurev-biochem-062917-012415.

59. Hashimoto, Y., Puddu, F., and Costanzo, V. (2011). RAD51- and MRE11-dependent reassembly of uncoupled CMG helicase complex at collapsed replication forks. Nat. Struct. Mol. Biol. *19*, 17–24. https://doi.org/10.1038/nsmb.2177.

60. Ceccaldi, R., Liu, J.C., Amunugama, R., Hajdu, I., Primack, B., Petalcorin, M.I.R., O'Connor, K.W., Konstantinopoulos, P.A., Elledge, S.J., Boulton, S.J., et al. (2015). Homologous-recombination-deficient tumours are dependent on Poltheta-mediated repair. Nature *518*, 258–262. https://doi.org/10.1038/nature14184.

61. Hoitsma, N.M., Norris, J., Khoang, T.H., Kaushik, V., Chadda, R., Antony, E., Hedglin, M., and Freudenthal, B.D. (2023). Mechanistic insight into AP-endonuclease 1 cleavage of abasic sites at stalled replication fork mimics. Nucleic Acids Res. *51*, 6738–6753. https://doi.org/10.1093/nar/gkad481.

62. Caldwell, C.C., and Spies, M. (2020). Dynamic elements of replication protein A at the crossroads of DNA replication, recombination, and repair. Crit. Rev. Biochem. Mol. Biol. *55*, 482–507. https://doi.org/10.1080/10409238.2020.1813070.

63. Schlacher, K., Christ, N., Siaud, N., Egashira, A., Wu, H., and Jasin, M. (2011). Double-strand break repair-independent role for BRCA2 in blocking stalled replication fork degradation by MRE11. Cell *145*, 529–542. https://doi.org/10.1016/j.cell.2011.03.041.

64. Mol, C.D., Izumi, T., Mitra, S., and Tainer, J.A. (2000). DNA-bound structures and mutants reveal abasic DNA binding by APE1 and DNA repair co-ordination [corrected. Nature *403*, 451–456. https://doi.org/10.1038/35000249.

65. Pellegrini, L., and Venkitaraman, A. (2004). Emerging functions of BRCA2 in DNA recombination. Trends Biochem. Sci. *29*, 310–316. https://doi.org/10.1016/j.tibs.2004.04.009.

66. Appleby, R., Joudeh, L., Cobbett, K., and Pellegrini, L. (2023). Structural basis for stabilisation of the RAD51 nucleoprotein filament by BRCA2. Nat. Commun. *14*, 7003. https://doi.org/10.1038/s41467-023-42830-1.

67. DeNizio, J.E., Liu, M.Y., Leddin, E.M., Cisneros, G.A., and Kohli, R.M. (2019). Selectivity and Promiscuity in TET-Mediated Oxidation of 5-Methylcytosine in DNA and RNA. Biochemistry *58*, 411–421. https://doi.org/10.1021/acs.biochem.8b00912.

68. Zámborszky, J., Szikriszt, B., Gervai, J.Z., Pipek, O., Póti, Á., Krzystanek, M., Ribli, D., Szalai-Gindl, J.M., Csabai, I., Szallasi, Z., et al. (2017). Erratum: Loss of BRCA1 or BRCA2 markedly increases the rate of base substitution mutagenesis and has distinct effects on genomic deletions. Oncogene *36*, 5085–5086. https://doi.org/10.1038/onc.2017.213.

69. Lim, P.X., Zaman, M., Feng, W., and Jasin, M. (2024). BRCA2 promotes genomic integrity and therapy resistance primarily through its role in homology-directed repair. Mol. Cell *84*, 447–462.e10. https://doi.org/10.1016/j.molcel.2023.12.025.

70. Hazan, I., Monin, J., Bouwman, B.A.M., Crosetto, N., and Aqeilan, R.I. (2019). Activation of Oncogenic Super-Enhancers Is Coupled with DNA Repair by RAD51. Cell Rep. *29*, 560–572.e4. https://doi.org/10.1016/j.celrep.2019.09.001.

71. Wang, D., Wu, W., Callen, E., Pavani, R., Zolnerowich, N., Kodali, S., Zong, D., Wong, N., Noriega, S., Nathan, W.J., et al. (2022). Active DNA demethylation promotes cell fate specification and the DNA damage response. Science *378*, 983–989. https://doi.org/10.1126/science.add9838.

72. Ronson, G.E., Starowicz, K., Anthony, E.J., Piberger, A.L., Clarke, L.C., Garvin, A.J., Beggs, A.D., Whalley, C.M., Edmonds, M.J., Beesley, J.F.J., and Morris, J.R. (2023). Mechanisms of synthetic lethality between BRCA1/2 and 53BP1 deficiencies and DNA polymerase theta targeting. Nat. Commun. *14*, 7834. https://doi.org/10.1038/s41467-023-43677-2.

73. Sale, J.E., Lehmann, A.R., and Woodgate, R. (2012). Y-family DNA polymerases and their role in tolerance of cellular DNA damage. Nat. Rev. Mol. Cell Biol. *13*, 141–152. https://doi.org/10.1038/nrm3289.

74. Srivastava, M., Su, D., Zhang, H., Chen, Z., Tang, M., Nie, L., and Chen, J. (2020). HMCES safeguards replication from oxidative stress and ensures error-free repair. EMBO Rep. *21*, e49123. https://doi.org/10.15252/embr.201949123.

75. Biayna, J., Garcia-Cao, I., Álvarez, M.M., Salvadores, M., Espinosa-Carrasco, J., McCullough, M., Supek, F., and Stracker, T.H. (2021). Loss of the abasic site sensor HMCES is synthetic lethal with the activity of the APOBEC3A cytosine deaminase in cancer cells. PLoS Biol. *19*, e3001176. https://doi.org/10.1371/journal.pbio.3001176.

76. Alexandrov, L.B., Kim, J., Haradhvala, N.J., Huang, M.N., Tian Ng, A.W., Wu, Y., Boot, A., Covington, K.R., Gordenin, D.A., Bergstrom, E.N., et al. (2020). The repertoire of mutational signatures in human cancer. Nature *578*, 94–101. https://doi.org/10.1038/s41586-020-1943-3.

77. Pfaffeneder, T., Spada, F., Wagner, M., Brandmayr, C., Laube, S.K., Eisen, D., Truss, M., Steinbacher, J., Hackner, B., Kotljarova, O., et al. (2014). Tet oxidizes thymine to 5-hydroxymethyluracil in mouse embryonic stem cell DNA. Nat. Chem. Biol. *10*, 574–581. https://doi.org/10.1038/nchembio.1532.

78. Kafer, G.R., Li, X., Horii, T., Suetake, I., Tajima, S., Hatada, I., and Carlton, P.M. (2016). 5-Hydroxymethylcytosine Marks Sites of DNA Damage and Promotes Genome Stability. Cell Rep. *14*, 1283–1292. https://doi.org/10.1016/j.celrep.2016.01.035.

79. Bhowmick, R., Minocherhomji, S., and Hickson, I.D. (2016). RAD52 Facilitates Mitotic DNA Synthesis Following Replication Stress. Mol. Cell *64*, 1117–1126. https://doi.org/10.1016/j.molcel.2016.10.037.

80. Groelly, F.J., Dagg, R.A., Petropoulos, M., Rossetti, G.G., Prasad, B., Panagopoulos, A., Paulsen, T., Karamichali, A., Jones, S.E., Ochs, F., et al. (2022). Mitotic DNA synthesis is caused by transcription-replication conflicts in BRCA2-deficient cells. Mol. Cell *82*, 3382–3397.e7. https://doi.org/10.1016/j.molcel.2022.07.011.

81. Prasad, R., Yen, T.J., and Bellacosa, A. (2021). Active DNA demethylation-The epigenetic gatekeeper of development, immunity, and cancer. Adv. Genet. (Hoboken) *2*, e10033. https://doi.org/10.1002/ggn2.10033.

82. Rošić, S., Amouroux, R., Requena, C.E., Gomes, A., Emperle, M., Beltran, T., Rane, J.K., Linnett, S., Selkirk, M.E., Schiffer, P.H., et al. (2018). Evolutionary analysis indicates that DNA alkylation damage is a byproduct of cytosine DNA methyltransferase activity. Nat. Genet. *50*, 452–459. https://doi.org/10.1038/s41588-018-0061-8.

83. Raderschall, E., Stout, K., Freier, S., Suckow, V., Schweiger, S., and Haaf, T. (2002). Elevated levels of Rad51 recombination protein in tumor cells. Cancer Res. *62*, 219–225.

84. Marzio, A., Puccini, J., Kwon, Y., Maverakis, N.K., Arbini, A., Sung, P., Bar-Sagi, D., and Pagano, M. (2019). The F-Box Domain-Dependent Activity of EMI1 Regulates PARPi Sensitivity in Triple-Negative Breast Cancers. Mol. Cell *73*, 224–237.e6. https://doi.org/10.1016/j.molcel.2018.11.003.

85. Aze, A., Sannino, V., Soffientini, P., Bachi, A., and Costanzo, V. (2016). Centromeric DNA replication reconstitution reveals DNA loops and ATR checkpoint suppression. Nat. Cell Biol. *18*, 684–691. https://doi.org/10.1038/ncb3344.

86. Schindelin, J., Rueden, C.T., Hiner, M.C., and Eliceiri, K.W. (2015). The ImageJ ecosystem: An open platform for biomedical image analysis. Mol Reprod Dev. *82*, 518–529. https://doi.org/10.1002/mrd.22489.

87. McQuin, C., Goodman, A., Chernyshev, V., Kamentsky, L., Cimini, B.A., Karhohs, K.W., Doan, M., Ding, L., Rafelski, S.M., Thirstrup, D., et al. (2018). CellProfiler 3.0: Next-generation image processing for biology. PLoS Biol. *16*, e2005970. https://doi.org/10.1371/journal.pbio.2005970.

88. Zivanov, J., Nakane, T., Forsberg, B.O., Kimanius, D., Hagen, W.J., Lindahl, E., and Scheres, S.H. (2018). New tools for automated high-resolution cryo-EM structure determination in RELION-3. eLife *7*, e42166. https://doi.org/10.7554/eLife.42166.

89. Zheng, S.Q., Palovcak, E., Armache, J.P., Verba, K.A., Cheng, Y., and Agard, D.A. (2017). MotionCor2: anisotropic correction of beam-induced motion for improved cryo-electron microscopy. Nat. Methods *14*, 331–332. https://doi.org/10.1038/nmeth.4193.

90. Rohou, A., and Grigorieff, N. (2015). CTFFIND4: Fast and accurate defocus estimation from electron micrographs. J. Struct. Biol. *192*, 216–221. https://doi.org/10.1016/j.jsb.2015.08.008.

91. Adams, P.D., Afonine, P.V., Bunkóczi, G., Chen, V.B., Davis, I.W., Echols, N., Headd, J.J., Hung, L.W., Kapral, G.J., Grosse-Kunstleve, R.W., et al. (2010). PHENIX: a comprehensive Python-based system for macromolecular structure solution. Acta Crystallogr. D Biol. Crystallogr. *66*, 213–221. https://doi.org/10.1107/S0907444909052925.

92. Emsley, P., and Cowtan, K. (2004). Coot: model-building tools for molecular graphics. Acta Crystallogr. D Biol. Crystallogr. *60*, 2126–2132. https://doi.org/10.1107/S0907444904019158.

93. Taglialatela, A., Alvarez, S., Leuzzi, G., Sannino, V., Ranjha, L., Huang, J.W., Madubata, C., Anand, R., Levy, B., Rabadan, R., et al. (2017). Restoration of Replication Fork Stability in BRCA1- and BRCA2-Deficient Cells by Inactivation of SNF2-Family Fork Remodelers. Mol. Cell *68*, 414–430.e8. https://doi.org/10.1016/j.molcel.2017.09.036.

STAR★METHODS

KEY RESOURCES TABLE

REAGENT or RESOURCE	SOURCE	IDENTIFIER
Antibodies		
Mouse Anti-phospho-Histone H2A.X (Ser139) (IF: 1:800)	Merck/Sigma	Cat#05-636; RRID:AB_309864
Rabbit CCDC111/PRIMPOL Polyclonal antibody (WB: 1:2500)	Proteintech	Cat#29824-1-AP; RRID:AB_2918349
Rabbit Recombinant Anti-SMUG1 antibody [EPR15624] (WB: 1:1000)	Abacam	Cat#ab192240
Mouse mAb Anti-BRCA2 (Ab-1) (2B) (WB: 1:1000)	Merck/Sigma	Cat#OP95; RRID:AB_2067762
Rabbit anti-RAD51 (D4B10) WB: 1:1000	Cell signaling	Cat#8875; RRID:AB_2721109
Mouse Monoclonal Anti-Vinculin WB: 1:20000	Merck/Sigma	Cat#V9131-100UL; RRID:AB_477629
Purified Mouse Anti-MEK2 (WB: 1:1000)	BD biosciences	Cat#610235; RRID:AB_397630
Polyclonal Rabbit anti-Human APEX1 / APE1 Antibody (WB: 1:1000)	LsBio	Cat#Ls-C116767; RRID:AB_10916102
Rabbit Anti-TDG antibody [EPR8774] (WB: 1:1000)	Abcam	Cat#ab154192; RRID:AB_3096877
Anti-ATR	Aze et al.[85]	N/A
Anti-MCM7 (Mouse monoclonal)	Santa Cruz	Cat#sc-9966
Anti-ORC1 (Mouse polyclonal)	Aze et al.[85]	N/A
Anti-RPA70 (Rabbit polyclonal)	Aze et al.[85]	N/A
Anti-CDC45 (Rabbit polyclonal)	Aze et al.[85]	N/A
Anti-RAD51 (Mouse monoclonal) [14B4]	Abcam	Cat#ab123
Anti-*Xenopus* POL α p180 (Mouse monoclonal) peptide antigen used: VKRLPAVTKPGH	Kolinjivadi et al.[32]	Abmart: clone 13026-1-3/C199
Anti-*Xenopus* POL δ 125 kDa (Mouse monoclonal) peptide antigen used: SSQTKKLRGDWDDD	Kolinjivadi et al.[32]	Abmart: clone 19570-1-1/C316
Mouse anti-HMCES (B-2) (WB: 1:1000)	Santa Cruz	Cat#sc-514238; RRID:AB_2813859
DNMT1 (D63A6) Rabbit mAb (WB: 1:1000)	Cell signaling	Cat#5032; RRID:AB_10548197
Chicken anti-Rat IgG (H+L) Cross-Adsorbed, Alexa Fluor 488 (IF: 1:200)	ThermoFisher Scientific	Cat#A-21470; RRID:AB_2535873
Goat anti-Rabbit IgG (H+L) Alexa Fluor 568 (IF: 1:200)	ThermoFisher Scientific	Cat#A11011; RRID:AB_143157
Donkey anti-Mouse IgG (H+L) Highly Cross-Adsorbed, Secondary Antibody, Alexa Fluor 568 (IF: 1:200)	ThermoFisher Scientific	Cat#A10037; RRID:AB_11180865
Rat monoclonal [BU1/75 (ICR1)] to BrdU (IF: 1:50)	Abcam	Cat#ab6326; RRID:AB_305426
Purified Mouse Anti-BrdU (B44) (IF: 1:50)	BD biosciences	Cat#347580; RRID:AB_10015219
Biological samples		
Xenopus egg extract	This manuscript	N/A
Chemicals, peptides, and recombinant proteins		
APE1	New England Biolabs	Cat#M0282S
APE1 inhibitor III	Sigma-Aldrich	Cat#262017
Auxin, (Indole-3-acetic acid sodium salt, IAA)	Sigma-Aldrich	Cat#I3750
Mirin	Sigma-Aldrich	Cat#M9948
O-2-Propynylhydroxylamine hydrochloride, (AA3 probe)	Sigma-Aldrich	Cat#SYX00221-1G
PFM01	Sigma-Aldrich	Cat#SML1735
POLθi	Schrempf et al.[21]	N/A
S1 nuclease	Sigma-Aldrich	Cat#N5661
S1 nuclease	Sigma-Aldrich	Cat#N5661
xSMUG1 protein	This manuscript	N/A

(Continued on next page)

Continued

REAGENT or RESOURCE	SOURCE	IDENTIFIER
xAPE1 protein	This manuscript	N/A
GST-BRC4	Hashimoto et al.[14]	N/A
Geminin	Aze et al.[85]	N/A
POLθ protein full length	Mann et al.[15]	N/A
Critical commercial assays		
CellTiter-Glo® Luminescent Cell Viability Assay	Promega	Cat#G7571
Click-iT™ EdU Cell Proliferation Kit for Imaging, Alexa Fluor™ 488 dye, Alexa Fluor™ 647 dye	ThermoFisher	Cat#C10337; CHEBI:52661 Cat#C10340;
CRISPR Gene Knockout Kit v2 targeting APEX1	Sinthego	N/A
DNeasy Blood & Tissue Kit	Qiagen	Cat#69504;
Lipofectamine CRISPRMAX Transfection Reagent	ThermoFisher	Cat#CMAX00003;
Nucleostain- DNA Damage Quantification Kit -AP Site Counting	Dojindo	Cat#DK02-12;
Qubit™ dsDNA HS Assay Kits	ThermoFisher Scientific	Cat#Q32854;
RNAiMax	ThermoFisher	Cat#13778150;
Deposited data		
Atomic Coordinates and CryoEM maps	Protein Data Bank (PDB) and Electron Microscopy Data Bank (EMDB)	PDB: 8RCD, 8RCF;EMDB: EMD-19050, EMD-19051
Images and graphs	Mendeley	Mendeley Data: https://doi.org/10.17632/2gjvrzddv7.1
Experimental models: Cell lines		
Human DLD-1 wild-type	Horizon	Cat#HD PAR-008; RRID:CVCL_0248
Human DLD-1 BRCA2−/−	Horizon	Cat#HD 105-007; RRID:CVCL_HD57
Human DLD-1 APEX1−/−	This manuscript	N/A
Human DLD-1 DNMT1NA	Scelfo et al.[45]	N/A
Human DLD-1 DNMT3B−/− DNMT1NA	Scelfo et al.[45]	N/A
Human PEO1 BRCA2Y1655X	Panzarino et al.[41]	N/A
Human C4-2 PEO1 BRCA2WT	Panzarino et al.[41]	N/A
Experimental models: Organisms/strains		
Xenopus laevis females	Nasco	LM00535MX
Xenopus laevis males	Nasco	LM00715MX
Oligonucleotides		
siAPOBEC3B	Horizon	Cat#L-017432-00-0005
siBRCA2	Horizon	Cat#L-003462-00-0010
siHMCES	Sigma	Cat#EHU036741-5UG
siMRE11A	Horizon	Cat#L-009271-00-0010
siPRIMPOL	Horizon	Cat#L-016804-02-0005
siSMUG1	Horizon	Cat#L-012838-01-0010
siTDG	Horizon	Cat#L-003780-01-0010
siTET2	Horizon	Cat#L-013776-03-0010
Universal control siRNA	Sigma-Aldrich	Cat#SIC001
siRAD51	Horizon	Cat#L-003530-00-0010
Recombinant DNA		
6His-pET-SMUG1	This manuscript	N/A
pGEX-6P-1-APE1	This manuscript	N/A
Mre11 BACMID vector pTP2620	Bhaskara et al.[33]	Addgene Cat#113311; RRID:Addgene_113311
Rad50 BACMID vector pTP813	Bhaskara et al.[33]	Addgene Cat#113308; RRID:Addgene_113308
RAD51	Appleby et al.[23]	N/A

(Continued on next page)

Continued		
REAGENT or RESOURCE	SOURCE	IDENTIFIER
Software and algorithms		
GraphPad Prism (version 9.3.0)	GraphPad	https://www.graphpad.com; RRID:SCR_002798
ImageJ version 2.3.0/1.53f	Schindelin et al.[86]	https://imagej.net; RRID:SCR_003070
CellProfiler 3.1.9	McQuin et al.[87]	https://cellprofiler.org; RRID:SCR_007358
Gatan Micrograph software	Gatan	N/A
Other		
Bioruptor	Diagenode	N/A
Electron microscopy grids	Ted Pella	https://www.tedpella.com/grids_html/
ChemiDoc MP	BioRad	N/A
EnVision microplate reader	PelkinElmer	N/A
FEI Tecnai 20 EM microscope equipped with GATAN high-resolution camera	FEI+Gatan	N/A
MED20 evaporator	Leica	N/A
Leica TCS SP8-STED confocal microscope	Leica	N/A
Olympus Upright BX61 fluorescence microscope	Olympus	N/A
Stratalinker equipped with 254 and 365 nm ultraviolet light bulbs	Stratagene	N/A
TLA100 rotor	Beckman	N/A

RESOURCE AVAILABILITY

Lead contact

Further information and requests for resources and reagents should be directed and will be fulfilled by the lead contact, Vincenzo Costanzo (vincenzo.costanzo@ifom.eu).

Materials availability

Materials generated in this study will be made available upon request by the lead contact.

Data and code availability

- The atomic coordinates and cryo-EM maps included in this study have been deposited in the Protein Data Bank and Electron Microscopy Data Bank (PDB 8RCD and 8RCF; EMDB EMD-19050 and EMD-19051). Original western blot and microscopy images have been deposited in Mendeley Data: https://doi.org/10.17632/2gjvrzddv7.1. All datasets are publicly accessible as the date of publication.
- This paper does not report any original code.
- Any additional information required to reanalyze the data reported in this paper is available from the lead contact upon request.

EXPERIMENTAL MODEL AND STUDY PARTICIPANT DETAILS

Xenopus laevis eggs

Eggs derived from *Xenopus laevis* frogs were used as an experimental model system. Collection of eggs from the female frogs was performed in a non-invasive way following chorionic gonadotropin (Sigma, CG10) injections. Once collected eggs were processed to obtain cytoplasm, which was incubated with sperm nuclei to start DNA replication reactions. Occasional surgical procedures were performed on the male frogs to harvest sperm nuclei. Experimental protocols were approved by the IFOM Animal Welfare committee and the Italian Ministry of Health. The number of animals used was kept to a minimum and was calculated taking into account the number eggs required to obtain the cytoplasmic extract needed for the experiments described. The animals were kept in highly regulated and monitored conditions with room and water temperature at 19 °C. Basic husbandry requirements were provided by the IFOM *Xl* facility.

Cell lines and culture

DLD-1 wild-type (DLD1^WT) and DLD-1 BRCA2-deficient cells (BRCA2^-/- cells,) were acquired from Horizon discovery. PEO1 cells bearing BRCA2^Y1655X mutation and the corresponding PEO1 reverted cells (C4-2) expressing BRCA2^WT protein were a gift from S. Cantor and T. Taniguchi. DLD-1, PEO1 and C4-2 cells were cultured in RPMI 1640 (Lonza) supplemented with 2 mM glutamine,

10% Fetal bovine serum (FBS) and 1% penicillin-streptomycin (Pen-Strep). Induction of DNMT1 degradation was archived by media supplementation with 500 μM of auxin (indol-3-acetic acid, IAA, SIGMA) for the time indicated in every figure. Cells were maintained at 37 °C and 5% CO_2. and were culture as described

Generation of DLD1 APEX1 knockout cell line

DLD1 APEX1 knockout cell line (hereinafter referred as DLD1 APEX1$^{-/-}$) was generated by CRISPR-Cas9 technology. DLD1 APEX1$^{-/-}$ cells were obtained by transient transfection of DLD1^{WT} cells with synthetic sgRNAs targeting APE1 and Cas9 protein (Synthego) with Lipofectamine CRISPRMAX Transfection Reagent (ThermoFisher) following manufacturer's instructions. Seventy-two hours after transfections cells were seeded for clonal selection, expanded and positive clones were confirmed by western blot analysis sanger sequencing analysis.

Generation of DLD1 DNMT1^{NA} and DNMT1^{NA} DNMT3B$^{-/-}$ cell lines

DLD1 DNMT1^{NA} and DLD-1 DNMT1^{NA} DNMT3B$^{-/-}$ cells were previously described.[45] Briefly, DLD1 DNMT1^{NA} cells were generated by electroporation of DLD1 WT and DNMT3B$^{-/-}$ cells expressing osTIR1-Myc9 with both the pX330 plasmid carrying a sgRNA targeting the ATG of DNMT1 and the donor template containing the mNeonGreen-AID tag by using the Lonza Nucleofector with Nucleofector Solution V following manufacturer's instructions. Five days after transfection, mNeonGreen positive cells were FACS sorted and seeded for clone isolation. Homozygous clones were expanded and confirmed by sanger sequencing, fluorescence microscopy and western blot analysis.

For DNMT3B knockout (DNMT3B$^{-/-}$) DLD1 cells expressing both osTIR1-Myc9 and Tet-inducible Cas9-AID were transduced with pSB700-H2B-ECFP-lentivirus expressing a sgRNA targeting the ATG of DNMT3B. ECFP-positive cells were FACS sorted and seeded for clonal selection and expansion. After 10 days of doxycycline induction, DNMT3B$^{-/-}$ clones were screened by PCR genotyping and immunofluorescence, and confirmed by western blot.

METHOD DETAILS

Expression and purification of recombinant proteins

Human wild-type RAD51 protein was expressed and purified as previously described.[23] Briefly, human RAD51 was co-expressed with His-MBP-BRCA2-BRC4 in *E.coli*. Cell pellets were resuspended in resuspension buffer (500 mM NaCl, 50 mM HEPES pH 7.4). Clarified cell lysate was loaded on a HisTrap HP 5 ml column pre-equilibrated with His Buffer A (20 mM HEPES pH 7.5, 300 mM NaCl, 5% glycerol) before isocratic elution in 40% His Buffer B (20 mM HEPES pH7.5, 300 mM NaCl, 5% glycerol, 500 mM imidazole). Eluate was diluted in A125 Buffer (20 mM HEPES pH7.5, 125 mM NaCl, 5% glycerol, 2 mM DTT) before loading on a pre-equilibrated HiTrap Heparin 5ml column and eluted in a gradient elution of 12.5% to 100% buffer A1000 (20 mM HEPES pH 7.5, 1 M NaCl, 5% glycerol, 2 mM DTT). Fractions containing RAD51 were concentrated before a final purification step by size exclusion using a Superdex200pg gel filtration column pre-equilibrated with RAD51 storage buffer (20 mM HEPES pH 7.5, 300 mM NaCl, 5% Glycerol, 2 mM DTT). Purified RAD51 was stored in small aliquots at -80°C.

Recombinant hMR was expressed and purified by the Biochemistry and Structural Biology Unit (BSU) at the European Institute of Oncology. The protein complex was expressed by co-infection of High Five Cells (BTI-TN-5B1-4) (ThermoFischer Scientific), with the baculovirus vectors pTP2620 encoding for hRAD50-HA-6His and pTP813 encoding for hMRE11-FLAG. The pTP2620 and pTP813 plasmids were a gift from Tanya Paull (Addgene #113311 and #113308 respectively). For protein purification pellets of infected cells were resuspended in lysis buffer (50 mM sodium phosphate pH 7, 500mM NaCl, 10% glycerol, 1mM DTT) supplemented with protease inhibitors cocktail Set III (Calbiochem), lysed by sonication and cleared by centrifugation at 70000 g for 45 min. The supernatant was loaded on a HisTrap HP column (Cytiva) using an AKTA chromatography system. The column was washed with a buffer containing 25 mM imidazole and was then eluted with an imidazole gradient from 25 mM to 500 mM in 10 column volumes. The resulting protein was concentrated and loaded on a Superose 6 column (Cytiva) pre-equilibrated in SEC buffer (50 mM HEPES, 150mM NaCl, 5% glycerol). Fractions containing monodisperse protein were concentrated in 50 kDa cut-off Amicon ultra centrifugal filters (Millipore) and flash frozen in liquid nitrogen for further assays.

POLθ protein purification was previously shown.[15] Briefly, Maltose Binding Protein (MBP)-tagged POLθ was expressed in insect cells following infection with the encoding baculovirus. Cell pellets were resuspended in MBP-lysis buffer (50 mM HEPES pH 7.6, 300 mM NaCl, 1 mM DTT, 1 mM EDTA) and cleared by centrifugation. The cleared lysate was loaded onto MBP-TRAP column (GE Healthcare), washed with 20 column volumes of washing buffer (50 mM HEPES pH 7.6, 300 mM NaCl, 1 mM EDTA, 5% glycerol); proteins were eluted with MBP-elution buffer (20 mM maltose, 50 mM HEPES pH 7.6, 200 mM NaCl, 1 mM EDTA, 5% glycerol). GST-BRC4 was purified as previously described.[14] Briefly, cDNA fragment encoding human BRC4 (amino acid 1511–1579 of BRCA2) cloned into pDONR221 (Invitrogen) were kindly provided by Dr F. Esashi (Oxford University). The fragment was then cloned into DEST15, an expression vector for GST-tagged recombinant proteins, using Gateway system (Invitrogen). The BRC4-DEST15 plasmid was transformed to BL21-AI cells, and recombinant GST-BRC4 protein production was induced by 0.2% (w/v) L-arabinose and purified with Glutathione Sepharose 4B according to standard procedures (GE Healthcare). GEMININ production was also previously described.[85] Briefly, 6xHistidine-tagged GEMININ (a gift from M Micheal) was expressed in BL21(DES) cells from a pET28 plasmid and purified on a nickel-NTA column (QUIAGEN) according to manufacturer instructions. GST-APE1 was

expressed in BL21(DE3) cells (Thermo Fisher Scientific. The protein expression was induced with 0.1 mM isopropyl-β-D-thiogalac-topyranoside (IPTG) and at 37 °C for 3 hours. The cells were then harvested by centrifugation and resuspended in lysis buffer (50 mM Hepes/NaOH pH7.5, 150mM NaCl, 1mM DTT) supplemented with protease inhibitors cocktail setIII (Calbiochem), lysed by sonication and cleared by centrifugation. The cleared lysate was incubated with Glutathione-Sepharose 4B resin (Cytiva), for 1 hour at 4 °C and then were loaded on a bench chromatography column. The resin was first washed with 30 vol of wash buffer containing 50 mM HEPES pH7.5, 500mM NaCl and 1 mM DTT, then with two vol. of PreScission cleavage buffer (50mM Tris-HCL pH7.6, 150mM NaCl, 1mM DTT, 1mM EDTA), finally the protein was excised from GST using PreScission Protease (GST-HRV 3C). The eluted protein was further purified by SEC on a Superdex 75 10/300 column (GE Healthcare) in PBS buffer.

6His-pET-SMUG1 was expressed in Bl21(DE3) cells. Cell pellets from cells expressing 6His-pET-SMUG1 were resuspended in His-lysis buffer (50 mM Hepes pH7.6, 300 mM NaCl,10% glycerol, 2-mercaptoethanol 0.25% Triton X100) supplemented with pro-tease inhibitors cocktail setIII (Calbiochem) and 12.5 U/ml Benzonase (Sigma), lysed by sonication and cleared by centrifugation. The cleared lysate was incubated with Talon metal affinity resin (Clontech) for 2 hours at 4 °C. The resin was then washed with 30 vol. of lysis buffer containing 500 mM NaCl and 10 mM Imidazole. The bound proteins were eluted with 300 mM imidazole in lysis buffer. The eluate was further purified by SEC on Superdex-75 column (GE Healthcare) preequilibrated in SEC buffer. Relevant fractions were concentrated in 50 kDa cut-off Amicon ultra centrifugal filters (Millipore).

Cloning

Human wild-type RAD51 protein was cloned as previously described.[23] The cDNA sequences encoding *Xl* APE1 and SMUG1 were obtained by RT-PCR, from RNA derived from *Xl* eggs with TRIzol Reagent (Thermo Fisher). The full-length APE1 sequence was ampli-fied by PCR using Phusion High-Fidelity DNA Polymerase (Thermo Fisher) and the primers xAPE1-Bam-For and xAPE1-Xho-Rev (see table). The PCR product was cloned into pGEX-6P-1 expression vector (Invitrogen). The sequence was verified by sequencing using the primers listed in the table below. The full-length SMUG1 sequence was also amplified by PCR using Phusion High-Fidelity DNA Polymerase (Thermo Fisher) and the primers xSMUG1-For and xSMUG1-Rev (see table). The PCR product was digested with restric-tion enzymes BamHI and XhoI (New England) and cloned into pET43-6H vector (Invitrogen) obtaining the 6His-pET-SMUG1. The sequence was verified through sequencing process using the primers listed in the table below.

The BACMID vectors pTP2620 and pTP813 to express recombinant wild type MRE11-RAD50 in Sf9 Cells used in this work were provided by Tania Paull through Addgene (Addgene #113311 and #113308, respectively)

xAPE1-Bam-For	GGGTTTGGATCCATGCCCAAGAGAGGGAAGAAGGAAAG
xAPE1-Xho-Rev	GGGTTTCTCGAGTCATATCGCCATAAGGAGTGTTATTGGA
xSMUG1-Bam-For	CGCGGATCCATGGCTGCGGAAGCTTGCGTG
xSMUG1-Xho-Rev	CCGCTCGAGCTATCAGCCAGTTAGTAAAGATAAAAC

DNA oligonucleotides for EMSA, SPR, and Cryo-EM

PAGE-purified DNA oligonucleotides were purchased from IDT and resuspended to 100 μM in TE buffer. dsDNA was annealed in TE buffer with equimolar concentration of each constituent strand of a duplex to a final concentration of 10 μM, by boiling at 95 °C for 5 minutes followed by slow cooling to room temperature. The names, tag status and sequences of the oligonucleotides are reported below, together with an indication of the experiments where they were used. The underlined X in the oligonucleotide sequence marks the presence of an AP site.

Name	Tag	Sequence (5' to 3')	Experiment		
			EMSA	SPR	Cryo-EM
AP0	Biotin	GGTATGCAGTGGTAGACGTGAGC	x	x	
AP1	Biotin	GGTATGCAGTG<u>X</u>TAGACGTGAGC		x	
AP3	Biotin	GGTATGCA<u>X</u>TG<u>X</u>TA<u>X</u>ACGTGAGC		x	
AP5	Biotin	GGTAT<u>X</u>CA<u>X</u>TG<u>X</u>TA<u>X</u>AC<u>X</u>TGAGC	x	x	x
AP7	Biotin	GG<u>X</u>AT<u>X</u>CA<u>X</u>TG<u>X</u>TA<u>X</u>AC<u>X</u>TG<u>X</u>GC			x
APc	-	GCTCACGTCTACCACTGCATACC	x		x

Electrophoretic mobility shift assays (EMSA)

EMSA reactions were prepared in the following buffer: 25mM HEPES pH 7.5, 150 mM NaCl, 2 mM DTT, 2 mM ATP, 5 mM CaCl$_2$. The oligonucleotides used in the assay were: AP0 (ssDNA), AP5 (abasic ssDNA), AP0+APc (dsDNA), AP5+APc (abasic dsDNA). The DNA

was added to a final concentration of 500 nM and incubated with increasing amounts of RAD51 corresponding to final protein concentrations of 1, 2.5, 5, 10, 20, 30 μM. Reactants were incubated at 25 °C for 15 minutes prior to loading. Immediately before loading, samples were mixed with a 0.5:1 volume of 50% (w/v) sucrose solution. Samples were run on a pre-run 0.5% agarose gel in 0.5xTB buffer (45 mM Tris, 45 mM boric acid) (2.5hr, 4 °C, 35V). After running, the gel was stained in a 2x SYBR Gold solution made up in MilliQ water (10 min, 25 °C), destained in MilliQ water (10 min, 25 °C), and imaged using a Typhoon FLA9000 by excitation at 473 nm.

Surface plasmon resonance (SPR)

Biacore T100 system (Cytiva) was washed twice with 1X HBS-E buffer (Cytiva) prior to coupling of the biotinylated DNA substrates on a Series-S sensor chip SA (Cytiva). The SA chip contains four flow cells that were used to couple the ssDNA oligos (AP0, AP1, AP3, AP5). The DNA oligos were prepared at final concentration of 100 nM in 150 μL of 1XHBS-E buffer. The DNA coupling process consisted of three injections with regeneration buffer (50 mM NaOH and 1 M NaCl) to activate the surface of the chip and remove any free or excess unbound streptavidin, followed by a pulse-mode injection of the DNA substrates into each flow cell at a flow rate of 10 μL/min and 10-second injection length. RAD51 samples at increasing final concentrations (100, 250, 500, 750, 1000, 2000, 3000, 5000 nM) were prepared in binding buffer (25 mM Hepes pH7.5, 100 mM NaCl, 5 mM $CaCl_2$, 5 mM $MgCl_2$, 1 mM ATP, 2 mM DTT) and injected sequentially from low to high concentration of RAD51. Binding response units were recorded at 20 μL/min for 240 seconds, injections were then stopped, a binding buffer wash started at the same flow rate and response units of dissociation were recorded for 360 seconds. DNA substrates and surface was regenerated by injecting regeneration buffer (25 mM Hepes pH 7.5, 1000 mM NaCl, 5 mM $CaCl_2$, 5 mM $MgCl_2$, 1 mM ATP, 2 mM DTT) at 100 μL/min for 120 seconds. The first-order association rate constants (K_{on}) were calculated from the slope of the linear fit of the 250 nM RAD51 binding curve in the 20 to 90 second interval after injection. Each binding experiment of the RAD51 concentration series was performed in triplicate.

Vitrification of RAD51 filament grids

RAD51 protein was thawed on ice and used to prepare a reaction mixture for grid freezing containing a final concentration of 5 μM RAD51 in reaction buffer: 150 mM NaCl, 25 mM HEPES pH 7.5, 2 mM DTT, 2 mM ATP, 5 mM $CaCl_2$, supplemented with 250 nM of either abasic ssDNA (AP7) or abasic dsDNA (AP5+APc). Reactions were incubated for 15 minutes at 25 °C prior to vitrification. UltrAuFoil R1.2/R1.3 300 mesh gold grids (Quantifoil) were glow-discharged twice for 1 minute using a PELCO easiGlow system (0.38 mBar, 30 mA, negative polarity). 3 μl of reaction mix was applied to each grid before plunge-freezing in liquid ethane using a Vitrobot Mark IV robot (FEI), set to 100% humidity, 4 °C, 2 second blot time and -3 blot force.

CryoEM data collection and processing

RAD51 grids were screened using a Talos Arctica 200 keV cryo transmission electron microscope (TEM) fitted with a Falcon 3 detector, and data were collected on a Titan Krios G3 CryoTEM fitted with a K3 detector using the EPU package (FEI). Grid preparation, screening and data collection were all performed at the CryoEM facility in the Department of Biochemistry, University of Cambridge. Data were stored and processed on the Cambridge Service for Data-Driven Discovery (CSD3) high-performance computer cluster using Relion 3.1.[88] Data collection parameters are reported in Table 1. Micrograph motion correction was performed using MotionCor2[89] and CTF estimation was performed using CTFFIND4.[90] Autopicking was performed based on manually picked 2D class averages with a picking threshold of 0.1 and the number of asymmetric units in the filament box size set to 6 (approximately one full turn of a filament). Autopicked particles were extracted with a box size of 200 Å for both CryoEM datasets and then binned 2x. 2D classification was performed iteratively on extracted particles with the option to ignore CTF correction until the first peak selected in addition to processing using 'fast subsets'. For the RAD51 filaments with single-stranded abasic DNA, 183,769 high-resolution particles were identified following 2D classification, which were used to generate an initial 3D model. 3D classification was performed with the helical reconstruction option turned on and starting values for the helical twist and helical rise of 56° and 16Å respectively. All 3D classes showed clear density for single-stranded DNA in the filament core with a noticeable gap in the density corresponding to the abasic site which repeated with every triplet. All 3D classes were selected, re-extracted and binned 2x. The 183,769 extracted particles were used to refine class 1 from 3D classification which was then globally sharpened in Relion 3.1 to a final resolution of 3.22 Å. For the RAD51 filaments with double-stranded abasic DNA, 169,548 high-resolution particles were identified following 2D classification. Generation of an initial 3D model and 3D classification was performed as described for the single-stranded DNA filament structure. All 3D classes showed clear density for duplex DNA in the filament core with a noticeable gap in the density corresponding to the abasic site which repeated with every triplet. Classes one and three were selected to continue further on the basis that they exhibited the clearest base-gap in the filament core. Selected particles from 3D classification were re-extracted and binned 2x. The 8853 extracted particles were used to refine class one from 3D classification which was then globally sharpened in Relion 3.1 to a final resolution of 3.43 Å.

Real-space refinement

Atomic models of the RAD51 NPFs with abasic ss- and dsDNA were built into the maps based on published structures of the pre- and post-synaptic RAD51 filaments (PDB IDs 8BQ2 and 8BR2, respectively). Filament models with 7 RAD51-ATP chains, 14 Ca^{2+} and one abasic DNA chain corresponding to the AP7 oligo (23 nucleotides), containing 7 regularly-spaced abasic sites (see DNA oligonucleotides for cryo-EM table); in addition, the filament model with abasic dsDNA contained the complementary DNA chain to AP7 (see

APc in DNA oligonucleotides for cryo-EM table). The model of abasic ssDNA NPF was refined against the post-processed map from Relion, whereas the model of the abasic dsDNA NPF was refined against the 3D refined map that had been sharpened using *phenix.local_aniso_sharpen* in PHENIX.[91] Restrains for the abasic nucleotide were generated using the Grade Web Server at: https://grade.globalphasing.org/cgi-bin/grade2_server.cgi. Real-space refinement was interspersed with manual modelling in Coot[92] to improve the fit of the model to the map. Refinement statistics[24,25] for the two filament models are reported in Table 1.

Egg extract and chromatin binding

Xl interphase egg extracts and sperm nuclei were prepared as previously described.[85] Briefly, *Xl* eggs were collected in MMR buffer (5 mM HEPES-KOH pH 7.5, 100 mM NaCl, 0.5 mM KCl, 0.25 mM $MgSO_4$, 0.5 mM $CaCl_2$, 25 μM EDTA) from chorionic gonadotropin injected female frogs. The eggs were de-jellied in 10 mM Tris pH 8.0, 110 mM NaCl and 5 mM DTT and rinsed three times in MMR. De-jellied eggs were released in interphase in presence of 5 μM Calcium Ionophore (A23187, Sigma) for 5-6 min, washed three times with MMR and rinsed twice in ice-cold S-buffer (50 mM HEPES-KOH pH 7.5, 50 mM KCl, 2.5 mM $MgCl_2$, 250 mM sucrose, 2 mM β-mercaptoethanol). Activated eggs were then packed by centrifugation at 1.200 rpm for 1 min and the excess of buffer was discarded. Eggs were crushed at 13.000 rpm for 12 min at 4 °C. The crude extract was collected and centrifuged at 70.000 rpm for 12 min at 4 °C in a TLA100 rotor (Beckman). The interphase extract was obtained by collecting and mixing the cleared cytoplasmic fraction together with the nuclear membranes. For sperm nuclei preparation 4 testis were removed from 2 male frogs and placed in petri dishes containing 10 mL EB buffer (50 mM KCl, 50 mM HEPES-KOH pH 7.6, 5 mM $MgCl_2$, 2 mM DTT). Testis were finely chopped with razor blade. The material was then transferred to 15 mL Falcon tube and spun at 2,000 x g, in a swinging bucket rotor for 5 min at 4 °C. The pellet was resuspended in a total volume of 2 mL of room temperature SuNaSp buffer (0.25 M sucrose, 75 mM NaCl, 0.5 mM spermidine, 0.15 mM spermine). To remove membranes 100 μl of 2 mg/ml lysolecithin (Sigma) were added and incubated for 10 min at room temperature. Reaction was stopped by adding 3% BSA (Sigma). The pellet was resuspended again in 2 mL EB and spun at 2,000 x g for 5 min at 4 °C. The final pellet was resuspended in 400 μl of EB + 30% glycerol. Sperm nuclei were tested for absence of DNA breaks with TUNEL assay as previously described.[85] Briefly, 20 μl of different sperm nuclei preparations (4000 n/μl) were incubated at 37 °C for 4 h in 170 μl H_2O supplemented with 20 μl 10 x TdT buffer (NEB), 90 U Terminal transferase (NEB) and 1 μl α-^{32}P-dCTP. Aliquots of the reaction were then precipitated with 5% TCA, 2% pyrophosphate solution and spotted on Whatman GF-C glass fiber filter. After ethanol washes, filters were dried and the incorporated TCA precipitable radioactivity was counted in scintillation counter. Sperm nuclei preparations with the lowest counts were used for all the experiments.

For chromatin binding 40 μl egg extract containing sperm DNA were isolated from master reactions treated as shown in Figure legends at the indicated time points. For immunoblotting, samples were diluted with 10 volumes of EB (100 mM KCl, 2.5 mM $MgCl_2$, and 50 mM HEPES–KOH pH 7.5) containing 0.25% NP-40 and centrifuged through a 0.5 M sucrose layer at 10,000 x g at 4 °C for 5 min. Pellets were washed once with EB and suspended in Laemmli loading buffer. Proteins were then resolved on an SDS-PAGE and monitored by WB.

In vitro enzymatic assays with DNA oligos
Enzymatic activity of xAPE1

All endonuclease experiments were performed *in vitro* using recombinant components.

100 nM of 5′ fluorescein-labeled single-strand oligo substrates 5'FAM-AP0 and 5'FAM-AP1 containing an AP site at the position marked by X (see oligo table below) were dissolved in reaction buffer containing 10 mM Tris-HCl pH 7.5, 50 mM NaCl, 10 mM $MgCl_2$, 1 mM DTT, and 5% of glycerol. DNA substrates and recombinant *Xl* APE1 protein were incubated for 5 min at 23°C. For these titration experiments, the reaction mix contained 5'FAM-AP0 or 5'FAM-AP1 DNA oligos and either buffer alone or dilutions of APE1 ranging from 25 nM to 400 nM. The reactions were then stopped by adding an equal volume of formamide loading buffer (95% formamide, 5 mM EDTA) and boiling for 5 min at 95°C. Samples were then resolved by running on 15% precast TBE-urea polyacrylamide denaturing gels (Criterion,Bio-Rad) at 100 V for 40 minutes. Gels were analyzed using the image processing software ImageJ.

Enzymatic activity of xSMUG1

250 nM of 5′ fluorescein-labeled single-strand oligo substrates 5'FAM-APU and 5'FAM-AP-AP were dissolved in reaction buffer containing 10 mM Tris-HCl pH 7.5, 50 mM NaCl, 10 mM $MgCl_2$, 1 mM DTT, and 5% of glycerol. DNA substrates and increasing concentrations of recombinant *Xl* SMUG1 protein (produced for this project) were pre-incubated for 20 min at 23°C before adding 200 nM of recombinant xAPE1. The reactions were incubated for 10 further minutes before being stopped by adding an equal volume of formamide loading buffer (95% formamide, 5 mM EDTA) and boiling for 5 min at 95°C. Samples were then resolved by running on 15% precast TBE-urea polyacrylamide denaturing gels (Criterion,Bio-Rad) at 100 V for 40 minutes. Gels were analyzed using the image processing software ImageJ. For these xSMUG1 titration experiments, the reaction mix contained DNA oligos (5'FAM-APU and 5'FAM-AP-AP) and either buffer alone or dilutions of xSMUG1 ranging from 25 nM to 200 nM. Gels were analyzed using the image processing software ImageJ.

Human MR- and APE1-mediated cleavage activity at AP sites

To test the MR AP-cleavage activity we used a method previously established.[34] Briefly, to obtain the AP substrate we used a 3'-end fluorescein labelled 50mer oligonucleotide (5'BIOT-3'FAM_50mer) (SIGMA) containing an uracil that was transformed in a AP site by treatment with uracil-DNA glycosylase (UDG) (NEB, M0282). 100 nM oligonucleotide was treated with 0.1 U/μl of UDG in UDG buffer (20 mM Tris, 1 mM DTT, 1 mM EDTA) for 10 min at 37 °C. 10μl of cleavage reaction containing 50 nM AP-oligonucleotide, 50-400 nM

MR in MR-reaction buffer (50 mM MOPS, 50 mM NaCl, 10 mM $MnCl_2$, 1 mM DTT) or 25-200 nM of recombinant human APE1 (APE1, NEB M0282) in NEB buffer-4, was incubated for 40 min at 37 °C. The reaction was ended by the addition of 1 μl of 10x STOP mix (2.5% SDS, 100 mM EDTA, 1 mg/ml Proteinase K) and incubation for 10 min at 37 °C. 10 μl of Gel Loading Buffer II (Thermo Fisher) containing 95% Formamide were added to the samples before separating the products on 15% Polyacrylamide-8M Urea gels. The signals were visualized with the iBRIGTH-1500 imaging system (Invitrogen) using the 455-485nm white EpiLED-illumination and the 508-557 emission filter. As standard-marker we used a 25 nM mix of the three fluorescein labelled oligonucleotides: 5'BIOT-3'FAM_U-50mer, 5'FAM_29mer and 3'FAM_20mer.

RAD51 protection against MR- or APE1-mediated cleavage of AP sites

100 μM 5'BIOT-3'FAM _U oligonucleotide was first treated with 0.1 U/μl UDG in UDG buffer for 10 min at 37 °C, then we added increasing amount of human RAD51(0.5 - 4 μM) in the presence of 1 mM AMP-PNP in a buffer containing (20 mM Tris, 50 mM NaCl, 2 mM $MnCl_2$,1 mM DTT) and incubated for further 20 min at 37 °C. Finally, we added MR at final concentration of 300 nM in MR-reaction buffer or or 300 nM of recombinant human APE1 (APE1, NEB M0282) in NEB buffer-4 and incubated for further 40 min at 37 °C. The reaction was ended by the addition of the STOP mix and the samples were processed as described above.

RAD51 protection against xSMUG1-mediated formation of AP sites

100 μM 5'FAM-APU_26mer oligonucleotide was first incubated with human RAD51(4 μM) in the presence of 1 mM AMP-PNP in a buffer containing (20 mM Tris, 50 mM NaCl, 2 mM $MnCl_2$,1 mM DTT) or with buffer alone for 30 min at 37 °C. The reactions was supplemented with 50 nM xSMUG1 or buffer and further incubated for 30 min 37 °C. The reactions was heat inactivated for 5 min at 95 °C. Finally, 400 nM xAPE1 was added and incubated for 30 min at 37 °C. The reaction was ended by the addition of the STOP mix and the samples were processed as described above.

Name	Sequence (5' to 3')
5'BIOT-3'FAM _U-50mer	**BIOT**-CAGAAAGGGAAAGTATACAACAAAAAGCA**U**CTCAAGTCTTGG AGAGAACA-**FAM**
5'FAM_29mer	**FAM**-CAGAAAGGGAAAGTATACAACAAAAAGCA
3'FAM_20mer	CTCAAGTCTTGGAGAGAACA-**FAM**
5'FAM-AP0_36mer	**FAM**-CAGTGCCGAAGCTTGTCAAGGTCCTGGAACTGACGT
5'FAM-AP1_36mer	**FAM**-CAGTGCCGAAGCTTGTC**X**AGGTCCTGGAACTGACGT
5'FAM-APU_26mer	**FAM**-CGCGAAACGCCTAG**U**GATTGGTAGGG
5'FAM-AP-AP_26mer	**FAM**-CGCGAAACGCCTAG**X**GATTGGTAGGG

DNA electron microscopy

DNA for electron microscopy analysis was processed as previously described with some modifications.[13,32,93] Briefly, for *Xl* replication intermediates preparation sperm nuclei (4000 n/μl) were incubated at 23 °C in 200 μl egg extract for 60 min, diluted with 400 μl of EB buffer, layered onto 800 μl EB-EDTA (EB buffer + 1 mM EDTA) + 30% (w/v) sucrose and centrifuged at 3,000 x g for 10 min at 4°C. Pellets were resuspended in 100 μl EB-EDTA and transferred to a 96-well plate. 4,5′,8-Trimethylpsoralen (TMP) was added at 10 μg/ml to each well. For human cells replication intermediates preparation 15x10⁶ cells were collected. After standard trypsinization, the cells were transferred to 15 ml Falcon tubes and spun down at 600 x g for 5 min at 4°C. The cell pellets were then washed once with 5 ml ice-cold PBS, resuspended in 10 ml ice-cold PBS and transferred to 10x5 mm Petri dishes, to which 10 mg/ml of TMP (Trimethylpsoralen, Sigma-Aldrich) were added and mixed. For EM on human genomic DNA 10-15 × 10⁶ cells were collected for each sample. The cells were trypsinized, transferred to 15 ml Falcon tubes, and centrifuged at 600 x g for 5 minutes. The cell pellet was then washed once with 5 ml of ice-cold 1X PBS, resuspended in 10 ml of ice-cold 1X PBS, and transferred to a Petri dish. *Xl* or human samples were incubated on ice for 5 min in the dark and irradiated with 365 nm ultraviolet light for 7 min on a precooled metal block. The procedure from TMP addition to irradiation with ultraviolet light was repeated four more times. Samples were then supplemented with 0.1% (w/v) SDS to lysate nuclei and treated with 100 μg/ml RNase A for 1 h at 37 °C. For complete protein digestion, psoralen-crosslinked chromatin was incubated with proteinase K (1 mg/ml) for 2 h at 50 °C. Genomic DNA was extracted by adding one volume of 1:1 (v/v) phenol–chloroform mixture, precipitated with isopropanol, washed with 70% ethanol and digested with 150 U PvuII HF restriction enzyme for 4 hours at 37 °C. To visualize DNA the samples were spread onto EM grids and stained as previously described.[13,32,93] Briefly, 50 ng DNA were resuspended in 5 μl of formamide supplemented with 0.4 μl of BAC solution (alkyl dimethyl benzyl ammonium chloride 0.2% w/v in formamide) diluted 1:10 (v/v) in water. The total volume was gently pipetted onto the surface of water in a Petri dish to form a film. DNA was transferred to carbon-coated EM grids (Ted Pella) by briefly allowing them to contact the surface of the DNA film using tweezers. After staining in 1% uranyl acetate solution followed by a brief wash in 100% ethanol, grids were air-dried on filter paper and then subjected to DNA carbon-platinum rotary shadowing with a Leica MED20. Image acquisition was obtained with a FEI Tecnai 20 EM microscope equipped with a GATAN high-resolution camera at the IFOM electron microscopy facility. Blind analysis of EM images was performed by EM specialists. Conversion of DNA length from nm to nucleotides was done considering 1 nt=0.34 nm under EM.

Chemical reagents

Aphidicolin was used at a concentration of 3 μM (M-APH) as indicated in figure legends. POLθi was previously described.[15,21] PMF01 was purchased from SIGMA (SML1735). POLθi and PFM01 were used at the concentrations indicated in the text and figure legend.

Antibodies

Anti-*Xl* proteins antibodies were previously described.[15,32,85] Rat monoclonal [BU1/75 (ICR1)] antibodies to BrdU (ab6326) were purchased from Abcam. Purified Mouse Antibodies against BrdU (B44) (347580) were from BD bioscience. Mouse Anti-phospho-Histone H2AX-Ser139 antibody was from Millipore (05-636). Anti-histidine was obtained from Sigma (SAB4301134).

The primary antibodies used against human proteins were as follows (maker and dilution are indicated in parenthesis: Anti-BRCA2 (Millipore, 1:1000), anti-DNMT1 (Cell Signaling, 1:1000), anti-PRIMPOL (Proteintech, 1:2500), anti-MRE11 (Cell signaling, 1:1000), anti-SMUG1 (Abcam, 1:1000), anti-RAD51 (Cell signaling, 1:1000), anti-APEX1 (LSBio, 1:500), anti-phospho-Histone H2A.X (Ser139, Millipore, 1:1000), anti-MEK2 (BD biosciences, 1:1000), and anti-Vinculin (Sigma, 1:20,000), anti-Tet2 (Invitrogen, 1:1000), anti-HMCES (Santa Cruz, 1:1000), anti-APOBEC3B (Abcam, 1:1000), anti-TDG (Abcam, 1:1000). After incubation with primary antibodies, appropriate horseradish peroxidase-conjugated secondary antibodies were applied for detection.

RNA interference

siRNA transfections were performed using Lipofectamine RNAiMax (ThermoFisher, 13778150) following manufacturer's instructions. The final concentration of siRNA was 25 nmol/L. The siRNAs used were Horizon smart pools against MRE11A (L-009271-00-0010), PRIMPOL (L-016804-02-0005), SMUG1 (L-012838-01-0010), TET2 (L-013776-03-0010), BRCA2 (L-003462-00-0010) and RAD51 (L-003530-00-0010), siTDG (L-003780-01-001), siAPOBEC3B (L-017432-00-0005) and HMCES (EHU036741-5UG) and universal control siRNA (SIC001) from Sigma. Knock down siRNA efficiency was assayed 48 hours after transfection by Western Blot analysis.

Cell viability assays

Twenty-four hours after transfection cells were seeded in a 96-well plates at density of 0.5-2x10^3 cells/well. POLθI, APEi III or AR03 was added 24 hours later at the indicated concentrations. Five days after, viability was assessed with the CellTiter-Glo Luminescent Cell Viability Assay (Promega) following manufacturer's instructions. Relative cell viability (%) was expressed as a percentage relative to the untreated (DMSO) cells. Each viability experiment was performed at least three times.

AP site quantification

AP sites in genomic DNA were quantified with DNA Damage Quantification Kit (Dojindo Molecular Technologies) following manufacturer's instructions. In brief, cells were treated as indicated and DNA was extracted with DNeasy Blood & Tissue Kit (Quiagen) supplementing the lysis buffer with RNase A at 1 μg/mL. Two micrograms of DNA were labeled with 5 mM of ARP probe 1h at 37 °C, purified through gel filtration and quantified using Qubit dsDNA HS (ThermoFisher). ARP in the labeled DNA was measured using an ELISA-like assay in a microtiter plate. The ARP-labeled DNA (30 ng in 60 μL) and 90 μL of DNA binding solution (Dojindo Molecular Technologies) were added to each well, and the plate was covered and incubated in the dark at 37 °C overnight. This was followed by incubation in 100 μL of HRP-Streptavidin solution (Dojindo Molecular Technologies) at 37 °C for 1 hour, and then Substrate Solution (Dojindo Molecular Technologies) at room temperature for 1 hour. Following addition of 100 μL of HCL 2N optical density (OD) measurements at 450 nm were then obtained from the wells. All ARP assays were performed in triplicate and the means were calculated. The data, expressed as the number of AP sites per 10^5 nucleotides, were calculated based on the linear calibration curve generated for each experiment using ARP-DNA standard solutions.

An alternative method based on AA3 as also used. Cells were seeded in 8-well chamber slides at 3 x 10^4 cells per well. The following day, cells were treated with AA3 (8 μM, Sigma-Aldrich), with or without APEi III (Sigma-Aldrich) or DMSO for 24 hours. To prepare the cells for immunofluorescence staining, they were pre-extracted with CSK100 buffer (100 mM NaCl, 10 mM PIPES pH 6.8, 3 mM MgCl$_2$, 300 mM sucrose, 0.5% Triton X-100) supplemented with 1 μg/mL of RNase A for 5 minutes on ice. Cell were then fixed and permeabilized with with methanol:acetone (1:1) for 5 minutes. AA3 incorporated on DNA was labeled with Alexa Fluor 647 azide using click chemistry (Click-it EdU Cell Proliferation Kit, ThermoFisher) following manufacturer's instructions. After a final wash with PBS, coverslips were incubated with 5 μg/mL DAPI in PBS for 10 minutes to stain the cell nuclei. The coverslips were then washed once and mounted in Vectashield plus mounting medium (Vector Labs). The slides were stored at 4 °C until image acquisition. Images were acquired with a Leica TCS SP8-STED confocal microscope with a 60X oil immersion objective 1.35 NA or 40X oil immersion objective. At least 10 images were captured per condition and more than 500 nuclei were analyzed with CellProfiler 4.1.3. For AP site detection in *Xl* nuclei were isolated through centrifugation in sucrose cushions and treated as above. ARP probe (Sigma A9723) was used instead of AA3.

Detection was obtained with Neutravidin DyLight 650 (Tehrmofisher 84607)

Western blotting

Cells were collected by trypsinization and lysed in RIPA lysis buffer (150 mM sodium chloride, 1% NP-40, 0.5% sodium deoxycholate, 0.1% sodium dodecyl sulfate, and 50 mM Tris, pH 8.0) supplemented with proteinase and phosphatase inhibitors. Whole-cell extracts were sonicated, quantified and boiled for 5 minutes at 55 °C in Laemmli buffer. Protein lysates were separated on precast

Midi-PROTEAN TGX 4%–20% gels (Bio-Rad). Subsequently, the proteins were transferred onto nitrocellulose membranes using the Trans-Blot Turbo system (Bio-Rad) and the high molecular weight program. The membranes were blocked with 5% milk in TBS + 0.1% tween for 1 hour. Following blocking, membranes were incubated overnight at 4°C with primary antibodies diluted in blocking buffer. After incubation with primary antibodies, appropriate horseradish peroxidase-conjugated secondary antibodies were applied for detection.

Cell immunofluorescence

Immunofluorescence analysis was performed as previously described[15] with minor modifications. In brief, cells were mock treated or treated with siRNAs against MRE11, BRCA2 or RAD51 as indicated in figure captions. Cells were then seeded on a glass coverslip or 8-well chamber slides, and after 24 hours, they were exposed to 2 μM POLθi, 10 μM PFM01 or APEI for 24 hours as indicated in figures. Following the drug treatment, cells were exposed to 10 μM EdU for 30 minutes. Subsequently, the cells were washed once with PBS and pre-extracted with CSK100 buffer (100 mM NaCl, 10 mM PIPES pH 6.8, 3 mM MgCl$_2$, 300 mM sucrose, 0.5% Triton X-100) for 2 minutes on ice. After another wash with PBS, the cells were fixed with 4% paraformaldehyde in PBS for 12 minutes at room temperature. Next, the cells were permeabilized with permeabilization buffer (0.2% BSA, 0.5% Triton X-100 in PBS) for 10 minutes, followed by a wash. The EdU-positive cells were detected using the Click-it EdU Cell Proliferation Kit (ThermoFisher) according to the manufacturer's instructions. The cells were then blocked with blocking solution (10 mM Glycine, 2% BSA, 0.2% gelatin, 50 mM NH$_4$Cl, 0.2% Triton X-100) for 1 hour at room temperature. Coverslips were incubated with the primary antibody for 1 hour at 37°C, followed by three washes with PBS. Subsequently, the coverslips/slides were incubated with the secondary antibody. After three additional washes with PBS, the coverslips were incubated with 5 μg/mL DAPI in PBS for 10 minutes, washed once, and mounted in Vectashield plus (Vector Labs). The mounted samples were stored at 4°C until image acquisition. Images were acquired with a Leica TCS SP8-STED confocal microscope with a 60X oil immersion objective 1.35 NA or 40X oil immersion objective. At least 10 images were capture per condition and more than 500 nuclei were analyzed with CellProfiler 4.1.3.

DNA fiber assay with S1 nuclease

Cells were seeded in 6-well dishes, and after 24 hours, the cells were pulse-labeled with 50 μM CldU (Sigma) for 20 minutes. The cells were then washed twice with warm PBS and labeled with 250 μM IdU (Sigma) for an additional 40 minutes. During the second pulse, a POLθ or APE inhibitor III (APE1i) were added. Alternatively, cells were labeled 48 hours post transfection with Control or specific siRNAs. After labeling, the cells were trypsinized, counted, and resuspended in CSK100 buffer (100 mM NaCl, 10 mM PIPES pH 6.8, 3 mM MgCl$_2$, 300 mM sucrose, 0.5% Triton X-100) at a final concentration of 1 x 10^6 cells/mL. The cells were permeabilized for 5 minutes at room temperature and then centrifuged at 7000 rpm for 5 minutes. The cell pellets were resuspended in 1 mL of S1 buffer (30 mM Sodium acetate pH 4, 2 mM Zinc sulfate, 50 mM NaCl, 5% glycerol). The exposed nuclei were incubated with 10 U/mL of S1 nuclease (Sigma) in S1 buffer. The nuclei were then centrifuged for 5 minutes at 7000xrpm, and the nuclei pellets were carefully washed once with 1 mL of PBS containing 0.1% BSA. After another centrifugation for 5 minutes at 7000xrpm, the nuclei were resuspended in PBS to a final concentration of 1-2 x 10^3 nuclei/μL. Two microliters of the cell suspension were lysed on a clean glass slide with 8 μL of MES lysis buffer (50 mM MES pH 5.6, 0.5% SDS, 50 mM EDTA) for 6 minutes. Subsequently, the slide was tilted at a 15-degree angle to allow the DNA to spread. The slides were air-dried for 30 minutes, fixed in freshly prepared acetic acid/methanol (1:3) for 10 minutes, and then air-dried and stored at 4 °C overnight. To prepare for immunodetection, the slides were rehydrated with 1x PBS for 5 minutes. The DNA was denatured with 2.5 M HCl for 60 minutes, followed by several washes with PBS. The slides were then blocked in blocking solution (5% BSA, 0.2% Triton X-100 in PBS) for 20 minutes. Next, the slides were incubated with a primary antibody mix consisting of anti-BrdU antibody (Abcam 6326, recognizing CldU) anti-BrdU antibody (BD Biosciences, recognizing IdU) both at a dilution of 1:50, in blocking solution for 90 minutes at 37°C in a humid chamber. After incubation, the slides were washed once with PBS 0.1% Tween and twice with PBS for 3 minutes each. Subsequently, the slides were incubated with a secondary antibody mix consisting of donkey anti-mouse Alexa 568 (1:150, ThermoFisher) and chicken anti-rat Alexa 488 (1:150, ThermoFisher) in blocking solution for 45 minutes at 37 °C in a humid chamber. The slides were then washed three times with PBS, air-dried, mounted in Vectashield plus (Vector Labs), and stored at 4 °C until image acquisition. Images were acquired using a Leica Thunder widefield microscope with a 63X oil immersion objective (1.35 NA). Approximately 10 to 15 images were captured per condition, and at least 200 fibers were measured using ImageJ software (version 2.3.0/1.53f). The experiments were repeated at least two times.

DNA fiber assay with APE1 nuclease

APE1 nuclease assay was essentially performed as the S1 assay with some modification. Permeabilized cells were centrifuged at 7000 rpm for 5 minutes and resuspended in 1mL APE1 buffer. Exposed nuclei were then incubated with 3 U/mL of recombinant human APE1 nuclease (NEB M0282) in APE1 buffer (50 mM Tris-HCl pH 8, 5 mM MgCl$_2$, 50 mM KCl, 5% glycerol) for 30 minutes at 37°C. Nuclei were centrifuged 5 minutes at 7000xrpm, nuclei pellets were carefully washed once with 1 mL of PBS 0.1% BSA, centrifugated 5 minutes at 7000 rpm and resuspend in PBS to a final concentration of 1-2x10^3 nuclei/μL. DNA was spread and stained as is the DNA fiber assay.

QUANTIFICATION AND STATISTICAL ANALYSIS

Statistical analysis

All experiments, if not indicated otherwise in the figure legend, were performed three times and representative experiments are depicted. No statistical methods or criteria were used to estimate sample size or to include/exclude samples. Statistical analysis was performed with GraphPad PRISM software (version 9.3.0) and Microsoft Excel. Statistical differences in the DNA fiber length analyses were determined using Kruskal-Wallis test followed by Dunn's post hoc test for multiple comparisons calculated on the median values of independent experiment data. Unpaired t-tests were used to assess the difference in means of two groups of data. One Way ANOVA followed Dunnet's post hoc analysis was used to compare each of several groups means against a single control group while One Way ANOVA followed by Tukey post hoc test was used to assess pairwise comparisons between group means. In all cases, ns indicates not significant, $*P<0.05$, $**P<0.01$, $***P<0.001$ and $****P<0.0001$. Image analysis was conducted using ImageJ and CellProfiler 4.1.3. Statistical details for each experiment including sample size, significance values and tests are indicated in figure legends and figures.